Dynamic equivalence conditions for an air-bearing simulator emulating scaled drag-free control dynamics

Mingwei Chen[1,2], Chu Zhang[1*], Jianwu He[1,2], Chao Yang[1], Li Duan[1,2], and Qi Kang[1,2]

[1] *Institute of Mechanics, Chinese Academy of Sciences, Beijing 100190, China;*
[2] *School of Engineering Science, University of Chinese Academy of Sciences, Beijing 100190, China*

The ground-based experimental tests are crucial to verify the related technologies of the drag-free satellite. This work presents a design method of the ground simulator testbed for emulating the planar dynamics of the space drag-free systems. In this paper, the planar dynamic characteristics of the drag-free satellite with double test masses are analyzed and non-dimensionalized. A simulator vehicle composed of an air bearing testbed and two inverted pendulums is devised on the basic of equivalent mass and equivalent stiffness proposed firstly in this paper. And the dynamic model of the simulator equivalent to the sensitive axis motion of the test mass and the planar motion of the satellite is derived from the Euler-Lagrange method. Then, the dynamic equivalence conditions between the space prototype system and the ground model system are derived from Pi theorem. To satisfy these conditions, the scaling laws of two systems and requirements for the inverted pendulum are put forward. Besides, the corresponding control scaling laws and a closed-loop control strategy are deduced and applied to establishing the numerical simulation experiments of underactuated system. Subsequently, the comparative simulation results demonstrate the similarity of dynamical behavior between the scaled-down ground model and the space prototype. As a result, the rationality and effectiveness of the design method are proved, facilitating the ground simulation of future gravitational wave detection satellites.

Drag-free satellite, Ground simulation, Pi theorem, Dynamical similarity, Scaling law

1.   Introduction

Since the drag-free control technology was proposed by Lange [1] in the 1960s, many scholars have conducted a lot of further research on it and proposed several important application prospects of drag-free satellites in earth gravity field measurement [2] and space gravitational wave detection [3-6] and other tasks. Space agencies around the world have performed lots of in-orbit experiments and completed corresponding space missions to verify a large number of relevant studies, such as GOCE satellite [7], GP-B satellite [8], Lisa-pathfinder (LPF) satellite [9] and Taiji-1 [10,11]. With the subsequent development of LISA project [12],

Taiji project [13] and Tianqin project [14], the drag-free control technology will become one of the critical researches of space gravitational wave detection and deep space exploration in the future.

For all kinds of spacecraft, including drag-free satellites, experimental verification is a necessary final step and perhaps the most crucial step. Because the related technologies must be rigorously demonstrated and verified before it can be used on space missions. One of the verification methods is to launch a test satellite, which is also the most direct way. In 2015, ESA launched the satellite LPF [9] to complete the drag-free control experiments to testify the relevant technologies of gravitational wave detection and gained the representative results. In 2019, the Chinese Academy of Sciences also launched Taiji-1 [10] and performed in-orbit experiments of single-degree-of-freedom drag-free control.

Kawano et al. [15] successfully completed the first in-orbit autonomous rendezvous docking flight using relative GPS navigation in the whole world.

Another verification method is using the simulator [16], which can be generally divided into two broad types: kinematics simulator and dynamics simulator. The ground kinematics simulators [16,17] can use the cartesian system, robotic manipulators and other simulator technologies to reproduce the spacecraft motion. Caon et al. [18] present a series of tests conducted on a custom robotic arm to reproduce many aspects of the spacecraft motion. Zong and Emami [19] developed an error compensation scheme to make the closed-loop ground manipulator have similar joint movements to those of the space manipulator. But the kinematics simulator can only be used to reproduce the kinematic and differential kinematic aspects of spacecraft motion. Different from the kinematics simulator, the dynamics simulator can simulate not only the kinematic and differential kinematic aspects but also at least a portion of the dynamic aspects of spacecraft motion. The dynamics simulators include microgravity orbit simulator [20], falling simulator [21] and ground dynamics simulator [22-27]. The ground dynamics simulators can achieve microgravity conditions using drop tower [22], air-bearing [22-26], suspension [27], and other methods [16,17,28].

All kinds of the simulators must satisfy the dynamic equivalence conditions [29], which make the dynamics of simulator equivalent to the dynamics of the space prototype system. The condition is described in Buckingham's Pi theorem (called Pi theorem) in Ref. [30], stating that all of the dimensionless Pi parameters have the same numerical values for both the prototype and the model. As a consequence, two systems are completely similar. Through the use of Buckingham's Pi theorem, Ciarcià et al. [24] reproduced the orbital relative dynamics of CW equation on a ground air-bearing testbed equivalent to the prototype system. The experimental results showed the dynamical similarity of the simulator with three degrees of freedom. Fernandez et al. [26] designed and developed a new granite hardware-in-the-loop air-bearing testbed that can emulate the relative orbital dynamics between two orbiting spacecraft. Eun et al. [25] devised a new state-of-the-art ground-based hardware-in-the-loop test facility, using linear/hemispherical air-bearings. And the experimental results verified the successful development of the entire facility for the spacecraft proximity operation strategy in the near future. Zappulla et al. [31] designed a state-of-the-art air-bearing testbed and performed a test campaign to showcase its capabilities and illustrate the testbed operations to develop guidance, navigation, and control methods for close-proximity operations. Using the air-bearing technology can operate the testbed for a long time, while other model simulators are too short to maintain the microgravity con-

dition. And test satellites have a higher cost, a higher risk and a longer cycle.

However, different from other spacecraft missions, drag-free control manipulates not only the absolute orbit motion of satellite but the relative motion between the satellite body and the test mass. As a result, it is extremely difficult to build a completely ground simulation model. For the performance index of the micro-thruster used in drag-free control, Yang et al. [28] designed a set of high-accuracy torsion pendulum device to measure the thrust response time of micro-thrusters on the ground. In addition, Zhang et al. [27] established a ground semi-physical drag-free control simulation system based on suspension pendulum and conducted closed-loop control experiments simulating the single-degree-of-freedom drag-free control.

The above research and the relevant research published at present barely mentioned the ground simulation of drag-free satellite with double test masses. Therefore, it is greatly challenging to design an equivalent model for the ground simulation. And for the future gravitational wave detection program, it is also necessary to provide a ground experimental platform for demonstration and verification of correlative techniques. Therefore, this paper presents a similarity design method of the drag-free satellite simulator based on dimensional analysis and Pi theorem. For emulating the planar dynamics behavior of the spacecraft, we designed an air-bearing spacecraft simulator testbed on a high-accuracy flat surface. The small angle rotation of two inverted pendulums equipped on the testbed can be theoretically equivalent to the sensitive axis motion of two test masses. Besides, dynamic equivalent conditions of the designed model are derived from similarity criterion as well as the corresponding scaling laws, which are applied on the closed-loop simulation model. In addition, A closed-loop control strategy for the underactuated model system is devised to complete simulation experiments of drag-free control under the displacement model. Finally, the simulation results of the scaling ground model are compared with that of the satellite according to the similarity relationship. It is expected to be verified that the dynamic behavior of the ground model is similar to that of the drag-free satellite with two test masses.

The paper is organized as follows: Section 2 describes the nondimensionalization of similarity criterion. Section 3 establishes the dynamic equivalent simulator model and scaling laws using Pi theorem. Section 4 reports the application of a control strategy, control scaling laws and thrust allocation. Section 5 discusses the similarity between two systems. Section 6 makes a conclusion.

2. Dimensional analysis of the prototype

According to description in Refs. [29,30], if a physical

phenomenon can be described by a dimensional equation of p variables with q fundamental units, the original equation could be rewritten in a nondimensional form by using $r = p - q$ dimensionless parameters. These dimensionless parameters generally called the "Pi" parameters and constitute similarity criterion of the system. In this section, the Pi parameters corresponding to the dynamic characteristics of the drag-free satellite with double test masses are deduced.

2.1 Dynamics model of the drag-free satellite with two test masses

Drag-free control means that the satellite utilizes the active control forces and torques generated by actuators to compensate the nonconservative disturbance forces acting on the satellite, which aims to make satellite body to track the free-falling test mass and maintain a relative static state without contact. Based on the concept of drag-free satellites, the space gravitational wave detection program [13] is planning to use three drag-free satellites with an equilateral triangle formation in orbit around the sun or the Earth. The conceptual model of a drag-free satellite with two test masses is shown in Fig. 1.

On the basic premise of rigid body dynamics, the motion model of the satellite with 6 degrees of freedom can be expressed as

$$\begin{bmatrix} \mathbf{M}'\ddot{\mathbf{r}}' \\ \mathbf{I}'\ddot{\boldsymbol{\varphi}}' \end{bmatrix} = \begin{bmatrix} \mathbf{f}' \\ \mathbf{l}' \end{bmatrix}, \tag{1}$$

where $\mathbf{M}'$ is the mass matrix of the satellite, and $\mathbf{I}'$ is the inertia matrix of the satellite. $\mathbf{r}'$ and $\boldsymbol{\varphi}'$ represent the displacement and rotation of the satellite body in the inertial coordinate system. $\mathbf{f}'$ and $\mathbf{l}'$ are external forces and moments exerted on the satellite, respectively. The test masses back-forward forces on the satellites can be ignored, because the back-forward forces on the satellites are much less than the external disturbance $\mathbf{f}'$ and $\mathbf{l}'$. The mass of the test masses is much less than the mass of the spacecraft. Without the change in the center of mass, each element of $\mathbf{M}'$ and $\mathbf{I}'$ remains constant.

Without deformation, the displacement and rotation of the test mass relative to the satellite body can be regarded as the displacement and rotation of the test mass relative to the electrode cage. Therefore, the dynamic model of the test mass is as follows:

$$\mathbf{M}'_{tm}\ddot{\mathbf{q}}'_{tm} + \mathbf{K}'\mathbf{q}'_{tm} = \mathbf{f}'_c + \mathbf{f}'_{tm} + \mathbf{f}'_d + \mathbf{M}'_{sc}\ddot{\mathbf{q}}'_{sc}, \tag{2}$$

where $\mathbf{M}'_{tm}$ is the generalized mass matrix of test masses. $\mathbf{q}'_{tm}$ is the position and attitude of test masses relative to the spacecraft body. $\mathbf{M}'_{sc}$ is the generalized sensitivity matrix of test masses relative to the absolute acceleration of the spacecraft. $\mathbf{q}'_{sc}$ is the absolute position and attitude of the
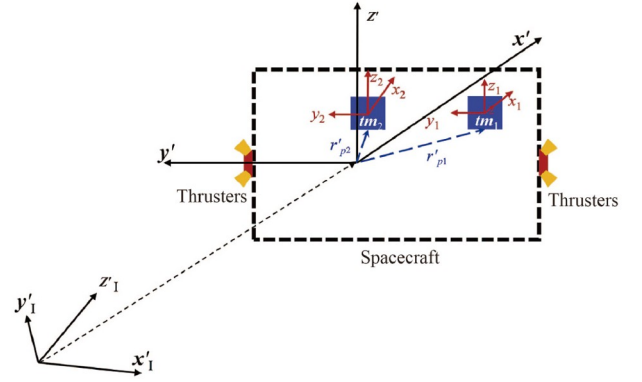

Figure 1 Diagram of the drag-free satellite with two test masses.

spacecraft. $\mathbf{K}'$ is the stiffness matrix of test masses. $\mathbf{f}'_c$ is the controlling forces and torques applied on test masses. $\mathbf{f}'_{tm}$ is the interaction forces acting on test masses. $\mathbf{f}'_d$ is the disturbance force exerted on test masses. For translational and rotational, Eq. (2) can be rewritten as

$$\begin{bmatrix} \ddot{\mathbf{r}}'_1 \\ \ddot{\boldsymbol{\varphi}}'_1 \\ \ddot{\mathbf{r}}'_2 \\ \ddot{\boldsymbol{\varphi}}'_2 \end{bmatrix} + \mathbf{K}' \begin{bmatrix} \mathbf{r}'_1 \\ \boldsymbol{\varphi}'_1 \\ \mathbf{r}'_2 \\ \boldsymbol{\varphi}'_2 \end{bmatrix} = \begin{bmatrix} \mathbf{f}'_1/\mathbf{m}'_1 \\ \mathbf{I}'^{-1}_1\mathbf{l}'_1 \\ \mathbf{f}'_2/\mathbf{m}'_2 \\ \mathbf{I}'^{-1}_2\mathbf{l}'_2 \end{bmatrix} + \mathbf{C}' \begin{bmatrix} -\mathbf{E} & \tilde{\mathbf{r}}'_{p1} \\ \mathbf{0} & -\mathbf{E} \\ -\mathbf{E} & \tilde{\mathbf{r}}'_{p2} \\ \mathbf{0} & -\mathbf{E} \end{bmatrix} \begin{bmatrix} \ddot{\mathbf{r}}' \\ \ddot{\boldsymbol{\varphi}}' \end{bmatrix}, \tag{3}$$

where $(\mathbf{r}'_1, \boldsymbol{\varphi}'_1)$ and $(\mathbf{r}'_2, \boldsymbol{\varphi}'_2)$ represent the displacement and rotation of the corresponding test mass with respect to the nominal position in the electrode cage, respectively. $\mathbf{f}'_i$ and $\mathbf{l}'_i$ are the external forces and torques applied to the test mass, respectively. $\mathbf{C}'$ is the coordinate-transformation matrix. $\tilde{\mathbf{r}}'_{pi}$ is the skew-symmetric cross product matrix, expressed as

$$\tilde{\mathbf{r}}'_{pi} = \begin{bmatrix} 0 & -z'_{pi} & y'_{pi} \\ z'_{pi} & 0 & -x'_{pi} \\ -y'_{pi} & x'_{pi} & 0 \end{bmatrix}, \tag{4}$$

where $\tilde{\mathbf{r}}'_{pi}$ is defined by the nominal position vector of the test mass 1 and 2 in the spacecraft body coordinate system, which is $\mathbf{r}'_{pi} = (x'_{pi}, y'_{pi}, z'_{pi})$.

2.2 Dynamics equation of the prototype system

With the limitation of the ground environment, the ground experiment cannot simulate the whole dynamics behavior of the drag-free satellite with full degrees of freedom. Therefore, this paper mainly studies the planar motion of the satellite and the sensitive axis motion of two test masses and establishes the corresponding drag-free control dynamics model.

From Eq. (1), the planar dynamic equation of the spacecraft is obtained as follows:

$$\begin{bmatrix} \ddot{x}' \\ \ddot{y}' \\ \ddot{\varphi}' \end{bmatrix} = \begin{bmatrix} F_x'/M' \\ F_y'/M' \\ T_z'/I_z' \end{bmatrix}, \tag{5}$$

where x' and y' represent the displacement and rotation of the spacecraft along x' and y' axis, respectively. φ' represents the rotation of the spacecraft along z axis. F_x' and F_y' are the resultant force along x and y axis applied to the spacecraft. T_z' is the torques along z axis applied to the spacecraft. I_z' is the inertia matrix of the satellite. On this basis, the plane schematic diagram of the test mass is shown in Fig. 2.

Subsequently, the translational dynamic equation of the i-th test mass is

$$\ddot{\mathbf{r}}_i' + \mathbf{K}_i'\mathbf{r}' = \frac{\mathbf{f}_i'}{\mathbf{m}_i} - \mathbf{C}_{i/\mathrm{SC}}\left(\ddot{\mathbf{r}}' - \tilde{\mathbf{r}}_{pi}\ddot{\boldsymbol{\varphi}}'\right), \tag{6}$$

where $\mathbf{C}_{i/\mathrm{SC}}$ is the coordinate transformation matrix. The expression is given in Eq. (A1).

Through deduction and simplification, the simplified dynamic equation of the sensitive axis motion of the test masses can be written as

$$\begin{aligned} \ddot{x}_1' + K_1'x_1' &= \frac{f_{2x}'}{m_1'} - \cos\varphi_1'\left(\ddot{x}' - y_{p1}'\ddot{\varphi}\right) - \sin\varphi_1'\left(\ddot{y}' + x_{p1}'\ddot{\varphi}'\right), \\ \ddot{x}_2' + K_2'x_2' &= \frac{f_{2x}'}{m_2'} - \cos\varphi_2'\left(\ddot{x}' - y_{p2}'\ddot{\varphi}\right) - \sin\varphi_2'\left(\ddot{y}' + x_{p2}'\ddot{\varphi}'\right). \end{aligned} \tag{7}$$

Regardless of the attitude change of the test mass with respect to the satellite, φ_1' and φ_2' are both the constant values. Thus, the similar dynamic characteristics of the prototype phenomenon are shown in Table 1.

2.3 Nondimensionalization of similarity parameter

According to Pi theorem, each Pi parameter corresponding to each variable in the prototype system is the product of this variable and q arbitrarily selected fundamental variables containing all of the fundamental units. Generally, the fundamental dimensions of the dynamic equation are time, length and mass. However, the two coordinate systems involved in the dynamic equations (5) and (7) are independent of each other, so the length dimension of the prototype system in Table 1 can be divided into two independent dimensions: L_{sc} and L_{tm}. On this base, there are 4 independent basic dimensions among the 27 system variables in the prototype system, including M, L_{sc}, L_{tm} and T.

In this paper, the chosen basic variables with all independent basic dimensions are M', x', x_1' and t'. Combined with other remaining variables in Table 1, the expression of dimensionless Pi parameter (π_i) is

$$\pi_i = M'^{\alpha_i}x'^{\beta_i}t'^{\gamma_i}P_i', \tag{8}$$

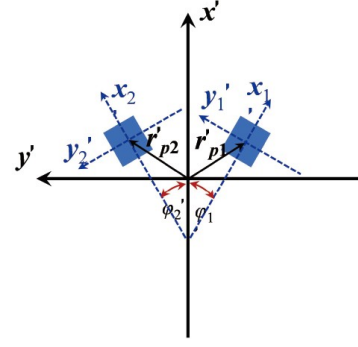where P_i' represents a variable apart from the four basic variables. The exponents of the fundamental variables in

Figure 2 Plane diagram of the drag-free satellite with two test masses.

Table 1 Physical parameters of the prototype[a]

Similar characteristic	Variables	Dimension
Inertial coordinate system	$x_{p1}', x_{p2}', y_{p1}', y_{p2}', x', y'$	$[L_{\mathrm{sc}}]$
Test mass coordinate system	x_1', x_2'	$[L_{\mathrm{tm}}]$
Time	t'	$[T]$
Mass	M', m_1', m_2'	$[M]$
Force	$F_x', F_y' \mid f_{1x}', f_{2x}'$	$[M\,L_{\mathrm{sc}}\,T^{-2}] \mid [M\,L_{\mathrm{tm}}T^{-2}]$
Acceleration	$\ddot{x}', \ddot{y}' \mid \ddot{x}_1', \ddot{x}_2'$	$[L_{\mathrm{sc}}\,T^{-2}] \mid [L_{\mathrm{tm}}\,T^{-2}]$
Stiffness	K_1', K_2'	$[T^{-2}]$
Torque	T_z'	$[M\,L_{\mathrm{sc}}^2\,T^{-2}]$
Rotational inertia	I_z'	$[M\,L_{\mathrm{sc}}^2]$
Attitude angle	φ'	1
Angle velocity	$\dot{\varphi}'$	$[T^{-1}]$
Angle acceleration	$\ddot{\varphi}_1'$	$[T^{-2}]$

a) The 27 variables construct the similar characteristics of the prototype system.

each Pi parameter are determined by the exponent of the remaining variable P_i'. And the dimension of P_i' need to be analyzed, as follows:

$$P_i' = M^{a_i}L_{\mathrm{sc}}^{b_i}T^{c_i} \quad \text{or} \quad M^{a_i}L_{\mathrm{tm}}^{b_i}T^{c_i}, \tag{9}$$

where L_{sc} and L_{tm} represent the length dimensions of variables x' and x_1', respectively.

The exponents α_i, β_i and γ_i in Eq. (8) are the appropriate integers to make π_i become a dimensionless parameter. Besides, a_i, b_i and c_i in Eq. (9) are dimensionless integers. Therefore, all exponents of π_i satisfy the following restricted relation:

$$\begin{cases} \alpha_i + a_i = 0, \\ \beta_i + b_i = 0, \\ \gamma_i + c_i = 0. \end{cases} \tag{10}$$

We can take the parameter x_{p1}' as an example. According to the dimensions of parameters in Table 1, it can be seen that $a_1 = 0$, $b_1 = 1$, $c_1 = 0$. Based on Eq. (10), it shows that $\alpha_1 = 0$, $\beta_1 = -1$ and $\gamma_1 = 0$. Consequently, the parameter π_1 can

be written as

$$\pi_1 = x'^{-1}x'_{p1}. \tag{11}$$

$$\pi_1=x'^{-1}x'_{p1}, \qquad \pi_2=x'^{-1}x'_{p2}, \qquad \pi_3=x'^{-1}y'_{p1}, \qquad \pi_4=x'^{-1}y'_{p2}, \qquad \pi_5=x'^{-1}y', \qquad \pi_6=x_1'^{-1}x_2'$$

$$\pi_7=M'^{-1}m_1', \qquad \pi_8=M'^{-1}m_2', \qquad \pi_9=M'^{-1}x'^{-1}t'^2 F_x', \quad \pi_{10}=M'^{-1}x'^{-1}t'^2 F_y', \quad \pi_{11}=M'^{-1}x_1'^{-1}t'^2 f_{1x}', \quad \pi_{12}=M'^{-1}x_1'^{-1}t'^2 f_{2x}',$$

$$\pi_{13}=x'^{-1}t'^2\ddot{x}', \qquad \pi_{14}=x'^{-1}t'^2\ddot{y}', \qquad \pi_{15}=x_1'^{-1}t'^2\ddot{x}_1', \qquad \pi_{16}=x_1'^{-1}t'^2\ddot{x}_2', \qquad \pi_{17}=t'^2 K_1', \qquad \pi_{18}=t'^2 K_2',$$

$$\pi_{19}=M'^{-1}x'^{-2}t'^2 T_z', \quad \pi_{20}=M'^{-1}x'^{-2}I_z', \qquad \pi_{21}=\varphi', \qquad \qquad \pi_{22}=t'\dot{\varphi}', \qquad \qquad \pi_{23}=t'^2\ddot{\varphi}'. \tag{12}$$

All of Pi parameters constitute the π group corresponding to the similar characteristics of the prototype system and establish the similarity criterion of the system. Due to that the π group defines the dynamic equivalence conditions, the model system must have the same π group exactly consistent with Eq. (12).

3. The scaled model with complete physical similarity

In order to reproduce the dynamic process of the prototype system in the ground experiment, a design method of an air floating model simulator is proposed. In this section, the constraint relationship of similarity criterion between the ground model system and the space prototype system is theoretically analyzed to ensure that the π group of the two systems are consistent with each other. And the principle of similarity is applied to deducing the scaling law, which determines that all parameters in the ground model can be correctly and reasonably scaled equivalently.

3.1 The dynamics model of the ground simulator system

The ground simulator is designed to be equivalent to the drag-free satellite. And the corresponding system dynamics model is theoretically derived through the use of Euler-Lagrange method.

3.1.1 The design of the ground simulator vehicle

The spherical air-bearing system allows the reproduction of three-degree-of-freedom attitude dynamics, while the planar air-bearing system has two degree-of-freedom translation and one degree-of-freedom rotation. In order to simulate microgravity environment and frictionless state of satellites, planar air-bearing technology is employed in designing a testbed, which could produce the smooth and steady air cushion between the testbed and the base surface. The schematic diagram of design is shown in Fig. 3.

In Fig. 3, the ground simulator vehicle is composed of the air-bearing testbed and two inverted pendulums. The angle between the plane projection of the inverted pendulum and the x-axis is φ_i, which is a constant. The centroid coordinate of the inverted pendulum is (x_{ci}, y_{ci}) and the position of the rotation shaft is (x_{pi}, y_{pi}). x_{pi} and y_{pi} are constants. The relationship between the two coordinates is as the following equations:

$$\begin{cases} x_{ci} = x_{pi} + e_i\sin\theta_i\cos\varphi_i, \\ y_{ci} = y_{pi} + e_i\sin\theta_i\sin\varphi_i, \end{cases} \tag{13}$$

where θ_i is the small angle of the inverted pendulum. e_i represents the distance between the center of mass and the axis of rotation of the inverted pendulum, which is a constant. Assuming that the experiment is carried out under the ideal condition, the friction force could be negligible. Therefore, the simplified dynamic model of the air-bearing testbed is expressed as

$$\begin{cases} \ddot{x} = F_x/M, \\ \ddot{y} = F_y/M, \\ \ddot{\varphi} = T_z/I_z, \end{cases} \tag{14}$$

where x and y represent the displacement and rotation of the air-bearing testbed along x and y axis, respectively. φ represents the rotation of the air-bearing testbed along z axis. F_x and F_y are the resultant force along x and y axis applied to the air-bearing testbed. T_z is the torques along z axis applied to the air-bearing testbed. I_z is the inertia matrix of the air-bearing testbed.
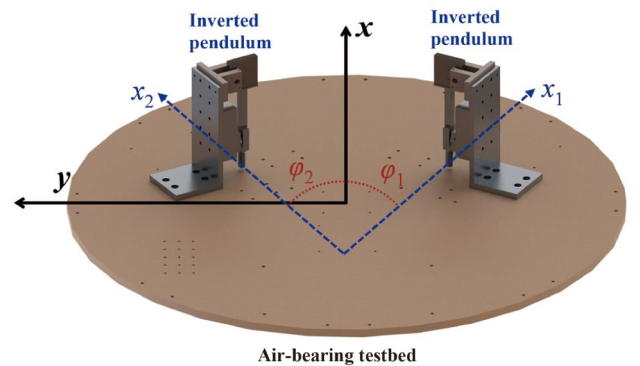

Figure 3 Ground simulator model.

In Fig. 3, two inverted pendulums are installed on the air-bearing testbed at the x-axis symmetrical position. The design model is shown in Fig. 4.

In Fig. 4, P_e is the center of mass of the inverted pendulum, and x_i is the displacement of the monitoring point on the inverted pendulum. d_i is the distance between the action point of force f_i and the rotation center of the inverted pendulum. L_i represents the distance between the monitoring point and the rotation center.

In addition, the inverted pendulum model is designed to reproduce the weak stiffness effect of the test mass. Assuming that the angle rotation of the inverted pendulum is enough small, we put forward the design concepts of the equivalent stiffness K_i and the equivalent mass $\tilde{m}_i$ ($i = 1, 2$) of the inverted pendulum.

K_i and $\tilde{m}_i$ are defined as follows:

$$\begin{cases} K_i = \dfrac{k_i - m_i g e_i}{J_i}, \\ \tilde{m}_i = \dfrac{J_i}{L_i d_i}, \end{cases} \tag{15}$$

where m_i is the mass of the i-th inverted pendulum. k_i is the rotational stiffness of the rotating shaft of the i-th inverted pendulum. J_i is the rotational inertia of the i-th inverted pendulum at the center of the rotating shaft. On this basis, the simplified dynamic model of two inverted pendulums is written as

$$\begin{cases} \ddot{x}_1 + K_1 x_1 = \dfrac{f_1}{\tilde{m}_1} - \cos\varphi_1\left(\ddot{x} - y_{p1}\ddot{\varphi}\right) - \sin\varphi_1\left(\ddot{y} + x_{p1}\ddot{\varphi}\right), \\ \ddot{x}_2 + K_2 x_2 = \dfrac{f_2}{\tilde{m}_2} - \cos\varphi_2\left(\ddot{x} - y_{p2}\ddot{\varphi}\right) - \sin\varphi_2\left(\ddot{y} + x_{p2}\ddot{\varphi}\right). \end{cases} \tag{16}$$

3.1.2 Deduction of the dynamic equation of the air-bearing testbed

The Euler-Lagrange method [32] is used to deduce the dynamic model of the above design from rigid body dynamics. The method can be written as

$$\frac{\mathrm{d}}{\mathrm{d}t}\frac{\partial L}{\partial \dot{r}} - \frac{\partial L}{\partial r} = F_r, \tag{17}$$

where r represents the system generalized displacement x, y, φ, θ_1, and θ_2. F_r is the system generalized force. And L is the lagrangian of the system, defined as the difference value between the kinetic energy T and the potential energy U.

Firstly, the kinetic energy T of the whole system needs to be calculated before establishing the dynamics model. The generalized displacement vector $\mathbf{r}_M$ of the platform is $(x, y, \varphi)^T$. And the generalized displacement vector of the i-th inverted pendulums is $\mathbf{r}_{mi}$, expressed as follows:

$$\mathbf{r}_{mi} = \begin{pmatrix} e_i\sin\theta_i\cos\varphi_i \\ e_i\sin\theta_i\sin\varphi_i \\ 0 \\ \theta_i \end{pmatrix} + \begin{vmatrix} 1 & 0 & -y_{ci} \\ 0 & 1 & x_{ci} \\ 0 & 0 & 1 \\ 0 & 0 & 0 \end{vmatrix} \mathbf{r}_M. \tag{18}$$
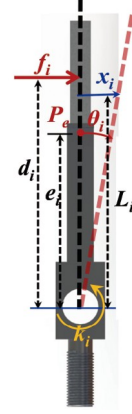

Figure 4   Model diagram of the inverted pendulum.

Hence, the system kinetic energy T can be described as

$$T = \frac{1}{2}\dot{\mathbf{r}}_M^T\mathbf{M}\dot{\mathbf{r}}_M + \frac{1}{2}\dot{\mathbf{r}}_{m1}^T\mathbf{m}_1\dot{\mathbf{r}}_{m1} + \frac{1}{2}\dot{\mathbf{r}}_{m2}^T\mathbf{m}_2\dot{\mathbf{r}}_{m2}. \tag{19}$$

The right three terms of the above formula are the kinetic energy of the testbed and the two inverted pendulums, respectively. $\mathbf{M}_{sc}$ and $\mathbf{m}_i$ are the generalized mass matrices of the testbed and the i-th inverted pendulum. $\dot{\mathbf{r}}_M$ and $\dot{\mathbf{r}}_{mi}$ are the generalized displacement vector of the testbed and the i-th inverted pendulum. Their expressions can be seen in Eq. (A2).

J_{mi} represents the rotational inertia of the i-th inverted pendulum around the center of mass. I_z represents the rotational inertia of the air-bearing testbed around the z axis. J_{mi} and I_z are both a constant value. I_{zi} represents the rotational inertia of the inverted pendulum around the z axis. The value of I_{zi} varies with the center of mass. Given that the inverted pendulum is regarded as a long bar with even distributed mass, I_{zi} can be as follows:

$$I_{zi} = \frac{1}{12}m_i e_i^2\sin^2\theta_i + m_i\Big[\left(x_{pi} + e_i\sin\theta_i\cos\varphi_i\right)^2 \\ + \left(y_{pi} + e_i\sin\theta_i\sin\varphi_i\right)^2\Big]. \tag{20}$$

Corresponding to the generalized coordinate $\mathbf{r} = (x, y, \varphi, \theta_1, \theta_2)^T$, the system kinetic energy T is rewritten as

$$T = \frac{1}{2}\dot{\mathbf{r}}^T\mathbf{M}\dot{\mathbf{r}} + \frac{1}{2}\dot{\mathbf{r}}^T\mathbf{A}_1^T\mathbf{M}_{cp}\mathbf{A}_1\dot{\mathbf{r}} + \frac{1}{2}\dot{\mathbf{r}}^T\mathbf{A}_2^T\mathbf{M}_{cp}\mathbf{A}_2\dot{\mathbf{r}}. \tag{21}$$

The first term on the right represents the kinetic energy of each degree of freedom, the second and third terms represent the kinetic energy generated by the coupled motion. The expressions of each matrix and each vector are shown in Eq. (A3).

The next step is to calculate the whole system potential energy U. The gravity potential energy is defined as zero if no displacement of the inverted pendulum generates. And supposing that the elastic potential energy only exists in the rotation shaft of inverted pendulum. Therefore, the system potential energy U is

$$U = \sum_{i=1}^{2} \frac{1}{2} k_i \theta_i^2 - m_i g e_i (1 - \cos\theta_i). \tag{22}$$

In consequence, the lagrangian L of the system can be written as the following formula:

$$L = T - U = \frac{1}{2} \dot{\mathbf{r}}^{\mathrm{T}} \mathbf{M} \dot{\mathbf{r}} + \frac{1}{2} \dot{\mathbf{r}}^{\mathrm{T}} \mathbf{A}_1^{\mathrm{T}} \mathbf{M}_{\mathrm{cp}} \mathbf{A}_1 \dot{\mathbf{r}} + \frac{1}{2} \dot{\mathbf{r}}^{\mathrm{T}} \mathbf{A}_2^{\mathrm{T}} \mathbf{M}_{\mathrm{cp}} \mathbf{A}_2 \dot{\mathbf{r}}$$
$$- \sum_{i=1}^{2} \left[\frac{1}{2} k_i \theta_i^2 - m_i g e_i (1 - \cos\theta_i) \right]. \tag{23}$$

Combined with Eq. (17), we can obtain the following expression:

$$\mathbf{F} = \frac{\mathrm{d}}{\mathrm{d}t} \frac{\partial T}{\partial \dot{\mathbf{r}}} - \frac{\partial T}{\partial \mathbf{r}} + \frac{\partial U}{\partial \mathbf{r}}. \tag{24}$$

Each term in Eq. (24) is

$$\mathbf{F} = \left(F_x - b_x \dot{x},\ F_y - b_y \dot{y},\ T_z - b_z \dot{\theta},\ f_1 d_1,\ f_2 d_2 \right)^{\mathrm{T}},$$
$$\frac{\partial T}{\partial \dot{\mathbf{r}}} = \mathbf{M}\dot{\mathbf{r}} + \mathbf{A}_1^{\mathrm{T}} \mathbf{M}_{\mathrm{cp}} \mathbf{A}_1 \dot{\mathbf{r}} + \mathbf{A}_2^{\mathrm{T}} \mathbf{M}_{\mathrm{cp}} \mathbf{A}_2 \dot{\mathbf{r}},$$
$$\frac{\partial T}{\partial \mathbf{r}} = \frac{1}{2} \dot{\mathbf{r}}^{\mathrm{T}} \frac{\partial \mathbf{M}}{\partial \mathbf{r}} \dot{\mathbf{r}} + \frac{1}{2} \dot{\mathbf{r}}^{\mathrm{T}} \frac{\partial}{\partial \mathbf{r}} \left(\mathbf{A}_1^{\mathrm{T}} \mathbf{M}_{\mathrm{cp}} \mathbf{A}_1 \right) \dot{\mathbf{r}} \tag{25}$$
$$+ \frac{1}{2} \dot{\mathbf{r}}^{\mathrm{T}} \frac{\partial}{\partial \mathbf{r}} \left(\mathbf{A}_2^{\mathrm{T}} \mathbf{M}_{\mathrm{cp}} \mathbf{A}_2 \right) \dot{\mathbf{r}},$$
$$\frac{\partial U}{\partial \mathbf{r}} = \left(0,\ 0,\ 0,\ k_1 \theta_1 - m_1 g e_1 \sin\theta_1,\ k_2 \theta_2 - m_2 g e_2 \sin\theta_2 \right)^{\mathrm{T}}.$$

By the use of the small-angle approximation principle, $\sin\theta_i$ is equivalent to θ_i so the small quantity can be ignored. The degrees of freedom of the testbed include x, y, φ. After simplification, the dynamic model of the air-bearing testbed is deduced as the following equations:

$$\begin{cases} F_x - b\dot{x} = \dfrac{\mathrm{d}}{\mathrm{d}t}\dfrac{\partial T}{\partial \dot{x}} - \dfrac{\partial T}{\partial x} = M\ddot{x} + \displaystyle\sum_{i=1}^{2} m_i\left(\ddot{x} - y_{pi}\ddot{\varphi} + e_i\ddot{\theta}_i\cos\varphi_i - e_i\dot{\theta}_i\dot{\varphi}\sin\varphi_i\right), \\[2mm] F_y - b\dot{y} = \dfrac{\mathrm{d}}{\mathrm{d}t}\dfrac{\partial T}{\partial \dot{y}} - \dfrac{\partial T}{\partial y} = M\ddot{y} + \displaystyle\sum_{i=1}^{2} m_i\left(\ddot{y} + x_{pi}\ddot{\varphi} + e_i\ddot{\theta}_i\sin\varphi_i + e_i\dot{\theta}_i\dot{\varphi}\cos\varphi_i\right), \\[2mm] T_z - b\dot{\varphi} = \dfrac{\mathrm{d}}{\mathrm{d}t}\dfrac{\partial T}{\partial \dot{\varphi}} - \dfrac{\partial T}{\partial \varphi} = I_z\ddot{\varphi} + \displaystyle\sum_{i=1}^{2}\left(I_{zi}\ddot{\varphi} + \dfrac{1}{2}\dot{I}_{zi}\dot{\varphi}^2\right) - \displaystyle\sum_{i=1}^{2} m_i y_{pi}\left(\ddot{x} - y_{pi}\ddot{\varphi} + e_i\ddot{\theta}_i\cos\varphi_i - e_i\dot{\theta}_i\dot{\varphi}\sin\varphi_i\right) \\[2mm] \quad + \displaystyle\sum_{i=1}^{2} m_i x_{pi}\left(\ddot{y} + x_{pi}\ddot{\varphi} + e_i\ddot{\theta}_i\sin\varphi_i + e_i\dot{\theta}_i\dot{\varphi}\cos\varphi_i\right) - \displaystyle\sum_{i=1}^{2} m_i e_i\dot{\theta}_i\sin\varphi_i\left(\dot{x} - y_{pi}\dot{\varphi} + e_i\dot{\theta}_i\cos\varphi_i\right) + \displaystyle\sum_{i=1}^{2} m_i e_i\dot{\theta}_i\cos\varphi_i\left(\dot{y} + x_{pi}\dot{\varphi} + e_i\dot{\theta}_i\sin\varphi_i\right). \end{cases} \tag{26}$$

In the third equation, the expression of $\dot{I}_{zi}$ is

$$\dot{I}_{zi} = 2m_i e_i \dot{\theta}_i \left(x_{pi}\cos\varphi_i + y_{pi}\sin\varphi_i \right). \tag{27}$$

The relationships between the testbed and the i-th inverted pendulum satisfies that $M \gg m_i$, $I_z \gg I_{zi}$, $i = 1, 2$. On the basis, only the first term on the right of Eq. (26) is kept. Besides, the friction force of the ground model can be ignored under the condition of air-bearing testbed. As a result, the second term on the left of Eq. (26) can be simplified so that the dynamic models (14) can be derived. This shows that the simulator testbed could be equivalent to the satellite platform.

3.1.3 Deduction of the dynamic equation of the inverted pendulum

With the same method, the dynamics model of the inverted pendulum could be derived from Eq. (24) as follows:

$$\begin{cases} f_1 d_1 = \dfrac{\mathrm{d}}{\mathrm{d}t}\dfrac{\partial L}{\partial \dot{\theta}_1} - \dfrac{\partial L}{\partial \theta_1}, \\[2mm] f_2 d_2 = \dfrac{\mathrm{d}}{\mathrm{d}t}\dfrac{\partial L}{\partial \dot{\theta}_2} - \dfrac{\partial L}{\partial \theta_2}. \end{cases} \tag{28}$$

Based on the small-angle approximation principle, we sort out the formula of the inverted pendulum, as follows:

$$\mathbf{D}\ddot{\boldsymbol{\theta}} + \mathbf{G}(\mathbf{r}, \dot{\mathbf{r}}) + \mathbf{K}\boldsymbol{\theta} = \mathbf{f} - \mathbf{C}_g \ddot{\mathbf{r}}_M, \tag{29}$$

where $\boldsymbol{\theta}$ is the rotation vector of the inverted pendulums. $\mathbf{f}$ is the generalized forces. $\mathbf{D}$ is the inertia matrix. $\mathbf{K}$ is the

stiffness matrix. Their expressions respectively are expressed as follows:

$$\boldsymbol{\theta} = \begin{pmatrix} \theta_1 \\ \theta_2 \end{pmatrix},\ \mathbf{f} = \begin{pmatrix} f_1 d_1 \\ f_2 d_2 \end{pmatrix},\ \mathbf{D} = \begin{bmatrix} J_1 & 0 \\ 0 & J_2 \end{bmatrix},\ J_i = J_{mi} + m_i e_i^2,$$
$$\mathbf{G}(\mathbf{r}, \dot{\mathbf{r}}) = \begin{bmatrix} G_1 & 0 \\ 0 & G_2 \end{bmatrix},\ \mathbf{K} = \begin{bmatrix} k_1 - m_1 g e_1 & 0 \\ 0 & k_2 - m_2 g e_2 \end{bmatrix}, \tag{30}$$

where $\mathbf{C}_g$ is the transformation matrix as shown in Eq. (A4). $\mathbf{G}(\mathbf{r},\ \dot{\mathbf{r}})$ contains Coriolis terms and centrifugal terms. By ignoring higher order small quantities, the expression of G_i is written as

$$G_i = 2m_i e_i^2 \varphi \dot{\theta}_i \dot{\varphi} + 2m_i e_i \dot{\theta}_i \theta_i \sin\varphi_i \left(\dot{y} + \dot{\varphi} x_{pi} \right)$$
$$+ 2m_i e_i \dot{\theta}_i \theta_i \cos\varphi_i \left(\dot{x} - \dot{\varphi} y_{pi} \right) + m_i e_i^2 \dot{\theta}_i^2 \theta_i$$
$$- \frac{7}{6} m_i e_i^2 \theta_i \dot{\varphi}^2 - m_i \dot{\varphi}^2 \left(e_i x_{pi}\cos\varphi_i + e_i y_{pi}\sin\varphi_i \right). \tag{31}$$

The ground simulator device meets the conditions, the same as conditions of the drag-free satellite in the scientific mode. First, the angular velocity of the testbed is extremely small. Second, the angle and angular velocity of the inverted pendulum are approaching 0. Thus, the Coriolis forces and centrifugalforces are negligible and Eq. (29) can be simplified as

$$\mathbf{D}\ddot{\boldsymbol{\theta}} + \mathbf{K}\boldsymbol{\theta} = \mathbf{f} - \mathbf{C}_g \ddot{\mathbf{r}}_M. \tag{32}$$

The small angle θ_i of the inverted pendulum can be transformed by the displacement x_i of the monitoring point

on the inverted pendulum. And the expression is $\theta_i = x_i/L_i$. Hence, Eq. (32) can be rewritten as follows:

$$\mathbf{L}\ddot{\boldsymbol{\theta}} = \mathbf{L}\mathbf{D}^{-1}\mathbf{f} - \mathbf{L}\mathbf{D}^{-1}\mathbf{K}\boldsymbol{\theta} - \mathbf{L}\mathbf{D}^{-1}\mathbf{C}_g\ddot{\mathbf{r}}_M,$$
$$\mathbf{L} = \begin{bmatrix} L_1 & 0 \\ 0 & L_2 \end{bmatrix}. \tag{33}$$

In order to establish the completely consistent π group with the prototype system, we apply the designed concepts of the equivalent stiffness K_i and the equivalent mass $\tilde{m}_i$ ($i = 1, 2$), which are defined as Eq. (15). As a result, Eq. (33) can be expressed as

$$\begin{pmatrix} \ddot{x}_1 \\ \ddot{x}_2 \end{pmatrix} = \begin{pmatrix} f_1/\tilde{m}_1 \\ f_2/\tilde{m}_2 \end{pmatrix} + \begin{bmatrix} K_1 & 0 \\ 0 & K_2 \end{bmatrix} \begin{pmatrix} x_1 \\ x_2 \end{pmatrix} + \mathbf{L}\mathbf{D}^{-1}\mathbf{C}_g\ddot{\mathbf{r}}_M. \tag{34}$$

In addition, a necessary requirement that transforms Eq. (16) to Eq. (34) must be satisfied. And this necessary requirement is about designing the inverted pendulum, as follows:

$$\mathbf{L}\mathbf{D}^{-1}\begin{bmatrix} m_1 e_1 & 0 \\ 0 & m_2 e_2 \end{bmatrix} = \mathbf{E}, \tag{35}$$

$\mathbf{E}$ is the identity matrix. By substituting Eq. (35) into Eq. (34), we can obtain the dynamic equation model (15).

Consequently, through the above theoretical analysis, the similarity between the small angle rotation of the inverted pendulum in the ground model and the sensitive axis movement of the test mass in the space drag-free control system can be properly verified.

3.2 The scaling laws

Let the principle of similarity applied to the dynamic equivalent conditions between the model system and the prototype system. It demands that the numerical values of model Pi parameters must be identical to that of the correspondent prototype Pi parameters. P represents the variable in the model system. The similarity criterion constraint relation between P' and P can be deduced from dynamic equivalent conditions, as the following expression:

$$M'^{\alpha_i} x'^{\beta_i} t'^{\gamma_i} P_i' = M^{\alpha_i} x^{\beta_i} t^{\gamma_i} P_i. \tag{36}$$

As a consequence, 23 similarity criterion constraints can be derived and written as follows:

$$\begin{aligned}
& x'^{-1}x_{p1}' = x^{-1}x_{p1}, && x'^{-1}x_{p2}' = x^{-1}x_{p2}, && x'^{-1}y_{p1}' = x^{-1}y_{p1}, && x'^{-1}y_{p2}' = x^{-1}y_{p2}, \\
& x'^{-1}y' = x^{-1}y, && x_1'^{-1}x_2' = x_1^{-1}x_2, && M'^{-1}m_1' = M^{-1}\tilde{m}_1, && M'^{-1}m_2' = M^{-1}\tilde{m}_2, \\
& M'^{-1}x'^{-1}t'^2 F_x' = M^{-1}x^{-1}t^2 F_x, && M'^{-1}x'^{-1}t'^2 F_y' = M^{-1}x^{-1}t^2 F_y, && M'^{-1}x_1'^{-1}t'^2 f_{1x}' = M^{-1}x_1^{-1}t^2 f_1, && M'^{-1}x_1'^{-1}t'^2 f_{2x}' = M^{-1}x_1^{-1}t^2 f_2, \\
& x'^{-1}t'^2\ddot{x}' = x^{-1}t^2\ddot{x}, && x'^{-1}t'^2\ddot{y}' = x^{-1}t^2\ddot{y}, && x_1'^{-1}t'^2\ddot{x}_1' = x_1^{-1}t^2\ddot{x}_1, && x_1'^{-1}t'^2\ddot{x}_2' = x_1^{-1}t^2\ddot{x}_2, \\
& t'^2 K_1' = t^2 K_1, && t'^2 K_2' = t^2 K_2, && M'^{-1}x'^{-2}t'^2 T_z' = M^{-1}x^{-2}t^2 T_z, && M'^{-1}x'^{-2}I_z' = M^{-1}x^{-2}I_z, \\
& \varphi' = \varphi, && t'\dot{\varphi}' = t\dot{\varphi}, && t'^2\ddot{\varphi}' = t^2\ddot{\varphi}.
\end{aligned} \tag{37}$$

In order to explicitly describe the constraint relationship constructed by the 23 equations in Eq. (37), the scaling factor associated to P' and P is introduced and defined as

$$\lambda_P = \frac{P}{P'}. \tag{38}$$

Based on the definition of the scaling factor, we can obtain all of the scaling laws corresponding to Eq. (37):

$$\lambda_{y_{p2}} = \lambda_{y_{p1}} = \lambda_{x_{p2}} = \lambda_{x_{p1}} = \lambda_y = \lambda_x,$$

$$\lambda_{x_2} = \lambda_{x_1}, \qquad \lambda_{m_1} = \lambda_{m_2} = \lambda_M, \quad \lambda_{F_x} = \lambda_{F_y} = \frac{\lambda_x \lambda_M}{\lambda_t^2},$$

$$\lambda_{f_{1x}} = \lambda_{f_{2x}} = \frac{\lambda_{x1}\lambda_M}{\lambda_t^2}, \quad \lambda_{\ddot{x}} = \lambda_{\ddot{y}} = \frac{\lambda_x}{\lambda_t^2}, \qquad \lambda_{\ddot{x}_1} = \lambda_{\ddot{x}_2} = \frac{\lambda_{x_1}}{\lambda_t^2}, \tag{39}$$

$$\lambda_{K_1} = \lambda_{K_2} = \frac{1}{\lambda_t^2}, \qquad \lambda_{I_z} = \lambda_x^2 \lambda_M, \qquad \lambda_{T_z} = \lambda_x \frac{\lambda_x \lambda_M}{\lambda_t^2},$$

$$\lambda_\varphi = 1, \qquad \lambda_{\dot{\varphi}} = \frac{1}{\lambda_t}, \qquad \lambda_{\ddot{\varphi}} = \frac{1}{\lambda_t^2}.$$

It is important to note that the π group is not unique, which is depended on the chosen fundamental variables. Different choices of fundamental variables result in different π groups. But the scaling laws determined by the dynamic similarity are unique and independent of the particular π group, which derive these laws. Because there are 4 independent factors among 27 scaling factors. And once numerical values of these 4 independent factors are set, the remaining 23 scaling factors are determined. Hence, the scaling laws play the key roles in physically correct scaling the testbed and two inverted pendulums.

3.3 The demands of the scaled model

To ensure that the model can reproduce the dynamic behavior of the prototype system in a similar way, the model must be scaled reasonably and correctly. And we need to choose the key scale factors involving all the basic units to design the ground experimental platform.

3.3.1 Demands of the basic scaling laws

In this paper, 4 independent scaling factors corresponding to the selected fundamental variables are λ_M, λ_x, λ_{x1} and λ_t. But more factors need to be considered. At first, the value of λ_{x1} is determined by the ratio between the real satellite size d_{sc}' and the designed testbed size $d_{simulator}$, as the following expression:

$$\lambda_{x_{p1}} = \frac{x_{p1}}{x_{p1}'} = \frac{d_{simulator}}{d_{sc}'}. \tag{40}$$

Secondly, the scaled testbed must float on the limited base surface. The scaling factor λ_x must satisfy

$$\lambda_x = \frac{x}{x'} \leqslant \frac{d_{float}}{\max(\Delta x_{max}', \Delta y_{max}')}, \tag{41}$$

$\Delta x_{max}'$ is the maximum displacement of satellite, the same as $\Delta y_{max}'$; "float" is the range of base surface. The above inequation means that the scaled motion must be accomplished on the base surface.

Thirdly, the mass M of the air-bearing testbed is designed in consideration of the bearing capacity M_{max} of the air bearing system. And the ratio between the value of M and the real satellite mass M' determines the mass scaling factor λ_M, which is limited by

$$\lambda_M = \frac{M}{M'} = \frac{m_i}{\widetilde{m}_i} \leqslant \frac{M_{max}}{M'}. \tag{42}$$

Then λ_{x1} is decided by the parameters of the inverted pendulum. The maximum displacement of the test mass in the direction of the sensitive axis is d_{max}'. And the rotation range of the inverted pendulum is set as $[-\theta_{max}, \theta_{max}]$. As a result, the maximum displacement of the sensor monitoring point is $L_i\theta_{max}$ by using the principle of small angle approximation. So, the scaling factor λ_{x1} can be expressed as

$$\lambda_{x_1} = \frac{x_1}{x_1'} \leqslant \frac{L_i\theta_{max}}{d_{max}'}. \tag{43}$$

Last, scaling factor λ_t can be determined by the active controlling forces. A certain interference force is exerted on the satellite in orbit around the Sun. and the satellite would produce the control forces to compensate the interference force. Assuming that the maximum control force provided by the space prototype system is F_{cmax}', we can obtain

$$M' a_{max}' = F_{cmax}'. \tag{44}$$

The maximum active control force provided by the actuator of the ground model system is F_{max} and the maximum acceleration a_{max} that the air-bearing testbed can reach is

$$a_{max} \leqslant \frac{F_{max}}{M}. \tag{45}$$

According to the definition of scaling factor and the scaling laws, a_{max} can be expressed as

$$a_{max} = \lambda_{\ddot{x}} a_{max}' = \frac{\lambda_x}{\lambda_t^2} a_{max}'. \tag{46}$$

Combining Eq. (45) with Eq. (46), we can derive

$$\lambda_t = \frac{t}{t'} \geqslant \sqrt{\frac{\lambda_M \lambda_x F_{cmax}'}{F_{max}}}. \tag{47}$$

Equations (40)-(43) and (47) constrain the values of four independent scaling factors corresponding to the chosen fundamental variable. As a consequence, scaling factors of the remaining variables can be computed.

3.3.2 Demands of the inverted pendulum

Aimed to be similar to the stiffness effect applying on the test mass in the prototype system, the equivalent stiffness K_i and the equivalent mass $\tilde{m}_i$ are constructed. The correspondent scaling laws λ_{K1}, λ_{K2}, λ_{m1} and λ_{m2} can be written as

$$\begin{cases} \lambda_{K_1} = \lambda_{K_2} = \frac{K_1}{K_1'} = \frac{K_2}{K_2'} = \frac{1}{\lambda_t^2}, \\ \lambda_{m_1} = \lambda_{m_2} = \frac{\widetilde{m}_1}{m_1'} = \frac{\widetilde{m}_2}{m_2'} = \lambda_M. \end{cases} \tag{48}$$

It can be seen that K_i and $\tilde{m}_i$ are depended on the scaling factors λ_t and λ_M, respectively. But the related parameters of K_i and $\tilde{m}_i$ include k_i, m_i, e_i, J_i and L_i, which decide the design of inverted pendulums. Hence, we put forward the following design requirements:

(1) The numerical values of λ_M and λ_t are decided by Eqs. (42) and (47). In addition, according to the definition (34) of K_i and $\tilde{m}_i$, the relations between the relevant parameters of the inverted pendulum can be described as follows:

$$\begin{cases} \frac{k_i - m_i g e_i}{J_i} = \frac{1}{\lambda_t^2} K_i', \\ \frac{J_i}{L_i d_i} = \lambda_M m_i'. \end{cases} \tag{49}$$

(2) π group of the inverted pendulum must be equivalent to that of the space prototype system. Consequently, it can be derived from Eq. (35) that the physical parameters of the inverted pendulum should also meet the following equation conditions:

$$\frac{m_i e_i L_i}{J_i} = 1. \tag{50}$$

Equations (49) and (50) constitute the necessary conditions for designing the inverted pendulum to keep the dynamic characteristics of the model system similar with that of the prototype system.

According to the analysis of the dynamic equivalence conditions and the establishment of the scaling laws, the scaled model can simulate the dynamic characteristics of capturing the test mass, as well as the displacement drag-free control and acceleration drag-free control. Hence, the air-bearing simulator platform installed with two inverted pendulums can reproduce the plane dynamic behavior of the drag-free satellite with double test masses. And the related drag-free control algorithms can be verified in the scaled model system.

4.   The simulation strategy

For verifying that the designed model is equivalent to the drag-free control system, the closed-loop control numerical simulation experiment is designed while it is an under-actuated system [33]. A closed-loop control strategy is proposed to keep the control stability of two systems. Besides, π theorem is applied to constructing the control scaling laws to keep the similarity between two closed-loop systems. Furthermore, we utilize the redundant thruster layout to manipulate the testbed, using a thrust allocation method.

4.1   The simulation strategy

Under the control mode of displacement, the satellite produces the active control forces to compensate the external interference force so that the satellite body is stationary relative to the test masses. In this process, there are five degrees of freedom involved, including x_1', x_2', x', y' and φ'. But the independent control quantities of the whole system are x', y' and φ'. It makes the simulation system become an underactuated system. Therefore, the closed-loop experiment needs a reasonable control strategy to guarantee that the five degrees of freedom of the whole system can all be controlled stably.

Corresponding to the satellite prototype system, there 5 degrees of freedom of the air bearing simulator testbed need to be controlled, involving x_1, x_2, x, y, and φ. And we intend to use redundant thrusters to control the degree of freedom x, y and φ. On this basis, the closed-loop control system and the simulation experiment verification strategy are established as shown in Fig. 5.

The set quantities x_{1d}', x_{2d}' and φ_d' of the space prototype system were scaled down and input into the ground closed-loop simulation system. The results of x_1, x_2, x, y and φ were scaled up and compared with the output results of the satellite to demonstrate the similarity of the dynamic beha-

viors of the two systems.

Similar to the spatial prototype system, the inverted pendulums are no longer controlled independently in the displacement control mode. As a result, the measured displacement x_1 and x_2 determine the displacement x, y and φ of the testbed tracking to the inverted pendulum. Through the analysis of Eq. (18), it can be seen that the coupling term of θ_i and φ varying with the change of the center of mass of the inverted pendulum is a high order small quantity so that it can be ignored. And given the existence of inertia, the relationship between the displacements x, y and φ and the measured displacements x_1 and x_2 can be deduced as follows:

$$\begin{pmatrix} x_1 \\ x_2 \end{pmatrix} = \mathbf{C}_{\mathrm{tr}} \begin{pmatrix} x \\ y \\ \varphi \end{pmatrix}, \tag{51}$$

where $\mathbf{C}_{\mathrm{tr}}$ represents the conversion relationship of displacement between air float platform and inverted pendulum. And the expression of $\mathbf{C}_{\mathrm{tr}}$ can be seen in Eq. (A5).

The inverted pendulum is installed on the testbed so that φ_{tm} is consistent with rotation angle φ of the testbed. Accordingly, Eq. (51) can be further written as

$$\begin{pmatrix} x_1 \\ x_2 \\ \varphi \end{pmatrix} = \begin{bmatrix} \mathbf{C}_{\mathrm{tr}} \\ 0 \quad 0 \quad 1 \end{bmatrix} \begin{pmatrix} x \\ y \\ \varphi \end{pmatrix}. \tag{52}$$

Through matrix inversion, x_1, x_2 and φ can be converted into the displacement x, y and φ required in the control system. Hence, we can obtain the input $\mathbf{e}_{\mathrm{input}}$ of the controller, expressed as follows:

$$\mathbf{e}_{\mathrm{input}} = \begin{pmatrix} e_x \\ e_y \\ e_\varphi \end{pmatrix} = \frac{\mathbf{B}}{\cos\varphi_1 \sin\varphi_2 - \cos\varphi_2 \sin\varphi_1} \begin{pmatrix} x_{1d} - x_1 \\ x_{2d} - x_2 \\ \varphi_d - \varphi \end{pmatrix}. \tag{53}$$

The matrix $\mathbf{B}$ is the result of matrix inversion. The expression is in Eq. (A6). x_{1d}, x_{2d} and φ_d are the designed values of x_1, x_2 and φ. System state can be observed by measuring x_1, x_2, x, y and φ.
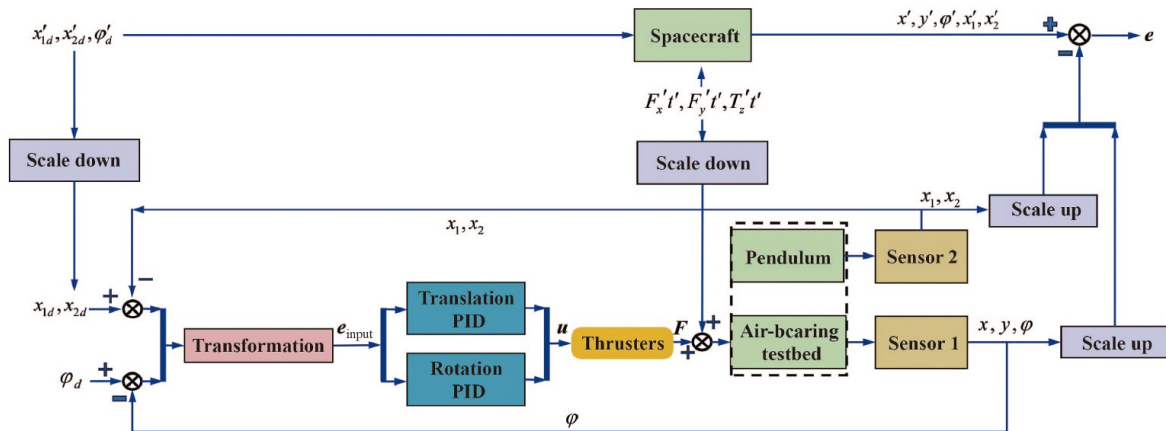

Figure 5   Simulation strategy of closed-loop control underactuated systems.

4.2 The control scaling laws

A very important and remarkable point in the above control strategy is that there is no independent control force exerted on the inverted pendulum along the sensitive axis in the simulation experiment. In addition, x_1, x_2 and φ are transformed into x, y and φ. As a consequence, the two coordinate systems x_1 and x are not independent with each other. It means that $\lambda_{x1} = \lambda_x$.

On this basis, the control scaling laws are derived from Pi theorem. The PID controller is utilized in the simulation experiment. The expression is as follows:

$$
\begin{cases}
F_x = K_{px}e_x(t) + K_{ix}\int_{t_0}^{t} e_x(\tau)\mathrm{d}\tau + K_{dx}\dot{e}_x(t), \\
F_y = K_{py}e_y(t) + K_{iy}\int_{t_0}^{t} e_y(\tau)\mathrm{d}\tau + K_{dy}\dot{e}_y(t), \\
T_z = K_{p\varphi}e_\varphi(t) + K_{i\varphi}\int_{t_0}^{t} e_\varphi(\tau)\mathrm{d}\tau + K_{d\varphi}\dot{e}_\varphi(t).
\end{cases}
\tag{54}
$$

Parameters K_{px}, K_{ix} and K_{dx} are the proportional, integral and differential coefficient of the controller along the x-axis, respectively, the same as K_{py}, K_{iy} and K_{dy} along the y-axis and $K_{p\varphi}$, $K_{i\varphi}$ and $K_{d\varphi}$ along the φ axis.

The output instructions of the controller involve forces and torques, the dimension of forces F_x and F_y are both $[M\,L_{sc}\,T^{-2}]$ and the dimension of T_z is $[M\,L_{sc}^2\,T^{-2}]$. The dimensions of the input commands e_x, e_y and e_z are $[L_{sc}]$, $[L_{sc}]$ and 1, respectively. The dimension of $\dot{e}_x$ and $\dot{e}_y$ are both $[L_{sc}\,T^{-1}]$. The dimensions of $\int e_x \mathrm{d}t$ and $\int e_y \mathrm{d}t$ are both $[L_{sc}\,T]$. To be consistent with the dimensions of the output orders, the dimensionsof the control parameters are deduced, as shown in Table 2.

Applying π theorem to controllers of the two systems, we can get the π group corresponding to the satellite control parameters, written as follows:

$$
\pi_{K_{px}} = M'^{-1}t'^2 K'_{px}, \quad \pi_{K_{py}} = M'^{-1}t'^2 K'_{py}, \quad \pi_{K_{d\varphi}} = M'^{-1}x'^{-2}_{p1}t'^2 K'_{d\varphi},
$$
$$
\pi_{K_{ix}} = M'^{-1}t'^3 K'_{ix}, \quad \pi_{K_{iy}} = M'^{-1}t'^3 K'_{iy}, \quad \pi_{K_{d\varphi}} = M'^{-1}x'^{-2}_{p1}t'^3 K'_{d\varphi},
$$
$$
\pi_{K_{dx}} = M'^{-1}t' K'_{dx}, \quad \pi_{K_{dy}} = M'^{-1}t' K'_{dy}, \quad \pi_{K_{d\varphi}} = M'^{-1}x'^{-2}_{p1}t' K'_{d\varphi}.
\tag{55}
$$

With the same deduction in Sect. 3.2, the control scaling laws of two systems are figured out, as follows:

$$
\lambda_{K_{px}} = \lambda_M \lambda_t^{-2}, \quad \lambda_{K_{py}} = \lambda_M \lambda_t^{-2}, \quad \lambda_{K_{d\varphi}} = \lambda_M \lambda_x^2 \lambda_t^{-2},
$$
$$
\lambda_{K_{ix}} = \lambda_M \lambda_t^{-3}, \quad \lambda_{K_{iy}} = \lambda_M \lambda_t^{-3}, \quad \lambda_{K_{d\varphi}} = \lambda_M \lambda_x^2 \lambda_t^{-3}, \tag{56}
$$
$$
\lambda_{K_{dx}} = \lambda_M \lambda_t^{-1}, \quad \lambda_{K_{dy}} = \lambda_M \lambda_t^{-1}, \quad \lambda_{K_{d\varphi}} = \lambda_M \lambda_x^2 \lambda_t^{-1}.
$$

Therefore, the control parameters of the ground model system can be calculated by using the scaled control parameters of the satellite closed-loop simulation system.

4.3 Thrust allocation

The thruster is generally taken as the actuator of the drag-free control system to manipulate the satellite. But redundant thrusters are usually configured to ensure control stability, due to the unidirectional characteristic of the thruster. To increase the similarity with the actual situation, the simulation is designed to use a redundant thruster layout. Furthermore, the control allocation [34] is introduced into the control algorithm to improve the computational efficiency and increase the stability of the system. Thus, the process of thrust allocation is involved in the simulation experiments. It means that the control instruction derived from the PID controller is input into the control allocation algorithm to compute the distribution instruction, which is executed by the thrusters. This process is shown in Fig. 6.

The unidirectional characteristic of thrusters causes a limitation of thrust range. To solve this problem, a hybrid optimal allocation algorithm is involved in the experiment. First step of this method is that the control instruction $\mathbf{u}$, calculated by the control law, are divided to the positive and negative, as follows:

$$
\begin{pmatrix} F_x \\ F_y \\ T_z \end{pmatrix} = \mathbf{u} = \mathbf{u}^+ + \mathbf{u}^-.
\tag{57}
$$

Secondly, we can calculate the efficiency matrix $\mathbf{A}$, which is defined by the redundant thruster configuration. Based on $\mathbf{A}$, we can work out the matrices $\mathbf{A}^+$ and $\mathbf{A}^-$, which are defined as the following formulas:

$$
\begin{cases}
\mathbf{A}\mathbf{A}^+ = \mathbf{E}, \\
\mathbf{A}\mathbf{A}^- = -\mathbf{E}.
\end{cases}
\tag{58}
$$

Then, each column $\mathbf{A}_i^+$ in $\mathbf{A}^+$ is computed by using the least square method,

Table 2   Dimensions of the control parameters

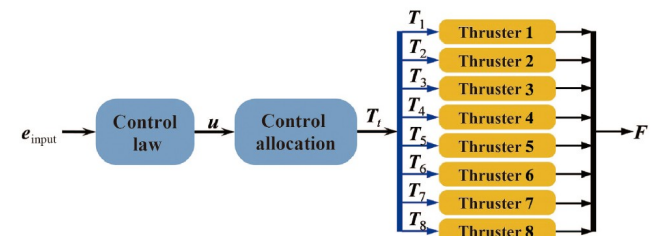| Control parameter	Dimension	Control parameter	Dimension
K_{px}, K_{py}	$[M\,T^{-2}]$	$K_{p\varphi}$	$[M\,L_{sc}^2\,T^{-2}]$
K_{ix}, K_{iy}	$[M\,T^{-3}]$	$K_{i\varphi}$	$[M\,L_{sc}^2\,T^{-3}]$
K_{dx}, K_{dy}	$[M\,T^{-1}]$	$K_{d\varphi}$	$[M\,L_{sc}^2\,T^{-1}]$

Figure 6   Process diagram of control allocation.

$$\min\left\{\left\|\mathbf{A}_i^+\right\|_2\right\}$$

$$\begin{cases} -\mathbf{A}_i^+ \leqslant \mathbf{0}, \\ \mathbf{A}\mathbf{A}_i^+ = \mathbf{E}_i, \end{cases} \tag{59}$$

where $\mathbf{A}_i^+$ represents the i-th column of $\mathbf{A}^+$. And $\mathbf{E}_i$ represents the i-th column of $\mathbf{E}$. After the matrix $\mathbf{A}^+$ is figured out, $\mathbf{A}^-$ can be obtained by using the same way. But it should be noted that the second constraint should be changed to $\mathbf{A}\mathbf{A}_i^- = -\mathbf{E}_i$.

Finally, the formula for calculating the thrust command through the matrix $\mathbf{A}^+$ and $\mathbf{A}^-$ is as follows:

$$\mathbf{T}_t = \mathbf{A}^+\mathbf{u}^+ - \mathbf{A}^-\mathbf{u}^-. \tag{60}$$

In the above formula, $\mathbf{A}^+\mathbf{u}^+ > \mathbf{0}$, $\mathbf{A}^-\mathbf{u}^- < \mathbf{0}$. Hence, each element of $\mathbf{T}_t$ must be greater than 0, which conforms to reality that actual thrust range of the cold air thruster is greater than 0.

5. The simulation results and analysis

In this section, all parameters and the basic scaling factors are designed according to the actual ground situation. And a redundant thruster layout is designed to apply to the simulation experiment.

Let us set the mass and size of the spatial prototype parameters. And compared with the similar experience, the mass and size both of testbed and the inverted pendulum are reasonably designed. Consequently, correspondent scaling factors can be determined. The relevant parameters and scaling factors are shown in Table 3.

Last scaling factor required in simulation system is λ_t, which determines the rest of other scaling factors. Different values of λ_t are designed for simulation verification. Given that $K_1 = K_2 = K$ and $K_1' = K_2' = K'$, the relevant parameters are shown in Table 4.

Combined with parameters and scaling factors designed in Tables 3 and 4, the results of the control scaling laws are shown in Table 5.

In the closed-loop simulation experiment, we intend to use 4 clusters of 8 adjustable cold gas thrusters as actuators of the drag-free control system. For using each thruster reasonably and sufficiently, a redundant thruster layout is designed and shown in Fig. 7.

As shown in Fig. 7, all the thrusters were paired and installed at 4 positions on the edge of the testbed. At each position, the angle between each one of paired thrusters and the horizontal symmetry axis is 45°. The thruster layout is always fixed and unchanged. The specific position and orientation are shown in Table 6.

The efficiency matrix $\mathbf{A}$ can be derived from the parameters in Table 6. Throughout the use of the hybrid optimal

Table 3 Basic parameters

Parameter of the prototype system	Designed value of the model system	Value of scaling factors
$M' = 500$ kg	$M = 100$ kg	$\lambda_M = 0.2$
$d_{sc}' = 3.2$ m	$d_{simulator} = 0.8$ m	$\lambda_{xp1} = \lambda_x = 0.25$
$x_i' = 1000$ μm	$x_i = 250$ μm	$\lambda_{x1} = 0.25$
$m' = 1.45$ kg	$\tilde{m}_i = 0.29$ kg	$\lambda_m = 0.2$
$I_z' = 640$ kg·m^2	$I_z = 8$ kg·m^2	$\lambda_{Iz} = 0.0125$

Table 4 Two groups of scaling laws

Group	Scaling law	Value	Parameters	Value
Group 1 ($\lambda_t = 1$)	λ_K	1	K (s^{-2})	−0.00015
			K (s^{-2})	−0.015
	λ_{Fx}	0.05	F_x' (μN)	100
			F_x (μN)	5
Group 2 ($\lambda_t = 0.1$)	λ_K	100	λ_K	1
			λ_{Fx}	0.05
	λ_{Fx}	5	K (s^{-2})	−0.00015
			F_x (μN)	5

Table 5 Control scaling laws

Values	Group 1	Group 2
λ_{Kpx}	0.2	20
λ_{Kpy}	0.2	20
$\lambda_{Kp\varphi}$	0.0125	1.25
λ_{Kix}	0.2	200
λ_{Kiy}	0.2	200
$\lambda_{Ki\varphi}$	0.0125	12.5
λ_{Kdx}	0.2	2
λ_{Kdy}	0.2	2
$\lambda_{Kd\varphi}$	0.0125	0.125
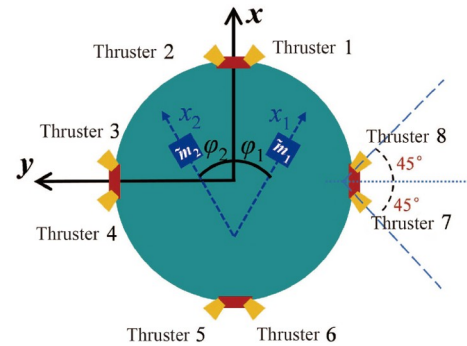
Figure 7 Thruster layout.

Table 6 Positions and orientations

Installation position	Orientation vector	
$\mathbf{p}_1 = (0.4$ m, 0)	$\boldsymbol{\tau}_1 = (0.707, -0.707)$	$\boldsymbol{\tau}_2 = (0.707, 0.707)$
$\mathbf{p}_2 = (0, 0.4$ m)	$\boldsymbol{\tau}_3 = (0.707, 0.707)$	$\boldsymbol{\tau}_4 = (-0.707, 0.707)$
$\mathbf{p}_3 = (-0.4$ m, 0)	$\boldsymbol{\tau}_5 = (-0.707, 0.707)$	$\boldsymbol{\tau}_6 = (-0.707, -0.707)$
$\mathbf{p}_4 = (0, -0.4$ m)	$\boldsymbol{\tau}_7 = (-0.707, -0.707)$	$\boldsymbol{\tau}_8 = (0.707, -0.707)$

allocation algorithm in Sect. 4.3, the matrix $\mathbf{A}^+$ and $\mathbf{A}^-$ can be deduced from the efficiency matrix $\mathbf{A}$. And the calculations of $\mathbf{A}$, $\mathbf{A}^+$ and $\mathbf{A}^-$ are shown in Eq. (A7).

$\mathbf{A}^+$ and $\mathbf{A}^-$ can be directly input into the closed-loop control system to calculate the thrust command efficiently. And we take the command $\mathbf{T}_t$ as the actual thrust in the simulation experiment. The efficiency matrix $\mathbf{A}$ can be used to map the thrust command directly to F_x, F_y and T_z, which compensate the impulse disturbance exerted on the testbed.

The steps in the simulation experiment are as follows:

(1) Establish the closed-loop control system in terms of Fig. 4.

(2) Input all of parameters in the satellite system. The values of interference forces along x-axis and y-axis are set to 100 μN, 100 μN. The moment along z-axis is 100 μN·m. The duration of action is 10 s.

(3) Adjust and record control parameters of the prototype system to realize the system stability control.

(4) Input scaled control parameters and scaled interference force impulse into the ground model for comparative test.

After debugging and adjustment, the control parameters of the space prototype and two groups of ground models are shown in Table 7.

Column 2 represents the parameters of prototype. Column 3 represents the parameters of Group 1. Column 2 represents the parameters of Group 2. Three sets of results according to the experimental steps are recorded.

First, the comparison between the experimental results of prototype and Group 1 is shown in Fig. 8.

The blue curve and red dash line in Fig. 8 represent the displacement simulation results of the space prototype and the ground model respectively. The blue solid line shows that although the closed-loop system in the displacement mode is stimulated by a certain impulse, the air-bearing testbed and the inverted pendulum can remain stable. The red dashed line indicates that the ground closed-loop system, designed on the basis of dynamic equivalent conditions and the control scaling law, can also maintain stability under the same control strategy. The first four diagrams show that the variation tendency of displacement x, y, x_1 and x_2 are consistent with that of the prototype system despite the inconsistent results. The cause is that the scaling law λ_x, λ_{x1} and λ_M are unequal to 1. The time scale factor λ_t of Group 1 is equal to 1. Consequently, two curves of φ' and φ in the fifth diagram are coincident.

Then we scaled up the above results according to scaling laws. The scaled results of the model system are compared with the results of the prototype system in Fig. 9.

The two overlapping curves in each picture indicate that the ground model variable scaled up is basically equal to the corresponding spatial prototype variable. It demonstrates the similarity between the ground model and the spatial prototype. Because the angle φ is a dimensionless variable, the fifth picture in Fig. 9 has no change, compared with the fifth picture in Fig. 8.

Second, the comparison between the simulation experi-

Table 7 Simulation experimental parameters

Parameters	Prototype	Group 1	Group 2
F_x (μN)	100	5	500
F_y (μN)	100	5	500
T_z (μN·m)	100	1.25	125
Duration (s)	10	10	1
Experiment time (s)	100	100	100
K_{px}	170	34	3400
K_{ix}	10.8	2.16	2160
K_{dx}	660	132	1320
K_{py}	170	34	3400
K_{iy}	10.8	2.16	2160
K_{dy}	660	132	1320
$K_{p\varphi}$	20	1.5	150
$K_{i\varphi}$	5.6	0.07	70
$K_{d\varphi}$	600	7.5	75

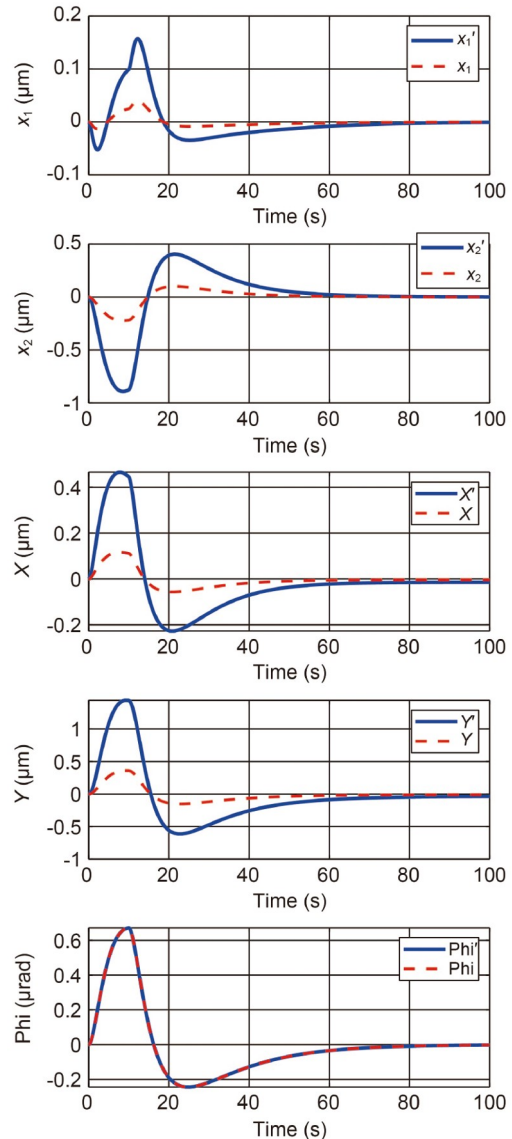**Figure 8** Results of prototype and Group 1.

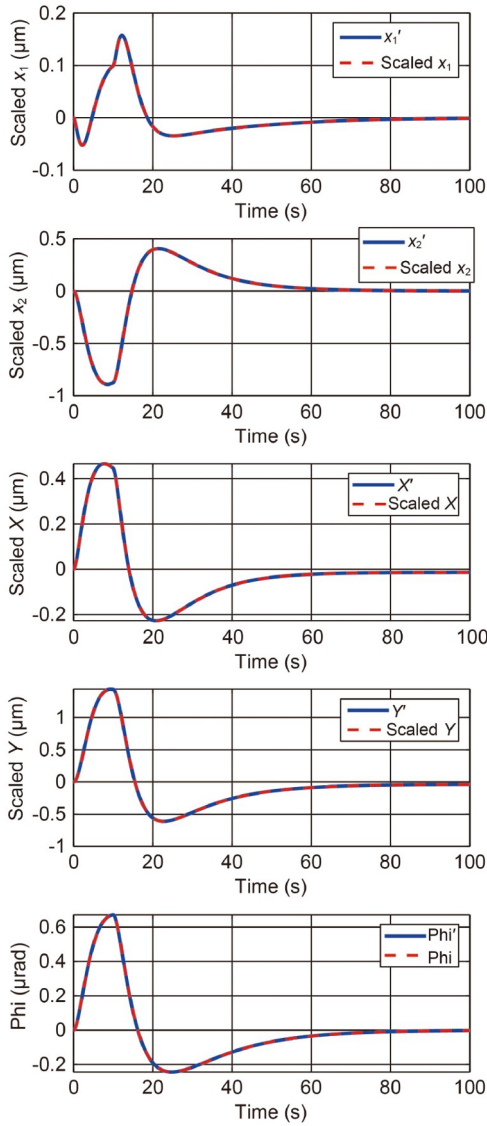**Figure 9** Results of prototype and scaled Group 1.

Figure 10 Results of prototype and Group 2.

ment results of prototype and Group 2 is shown in Fig. 10.

The blue lines in Figs. 8 and 10 represent the same simulation results of the prototype system. The red dashed line in Fig. 10 represents the simulation experiments of the Group 2. The above results show that the ground model system of the Group 2 stimulated by the scaled impulse can reach a stable state faster than both Group 1 and the prototype. Besides, the amplitudes of two groups are basically consistent with each other, which indicates that changing the time scale factor cannot change the displacement amplitude.

In the simulation experiment of Group 2, all but one of 4 basic scale factors is the same as Group 1. The difference is that $\lambda_t = 0.1$. Because both kinematic similarity and dynamic similarity must be satisfied, we need to compare the results of the two systems at the homologous time. As a result, the whole simulation time of the space prototype simulation and the first 10 s of the ground model simulation need to be

normalized. Then, the data of the Group 2 simulation within the first 10 s can be scaled up according to the scaling laws. The corresponding consequences are compared with the prototype system, as shown in Fig. 11.

The above pictures show that the scaled displacement curve of the ground model could overlap the corresponding displacement curve of the space prototype after time normalization. It indicates that homologous points of two systems lie at same positions at homologous time. And the same tendency reveals that the homologous masses experience homologous forces at homologous time. In addition, difference of λ_t between two groups has no influence on the system stability.

In order to simulate the space system more realistically, the thruster noise and sensor noise are introduced into the ground model system. The noises are formed by using the existing thruster noise index requirement [9,10,28] com-

bined with the noise discrete shaping filter. The Band-limited White Noise in Simulink is used to simulate the white noise of the specified frequency. The produced white noise can be turned into the coloured noise through the noise discrete shaping filter modeled by transfer function. The coloured noises are used as the input of the system. And the noises of the sensors or thrusters can be formed by the white noise and the shaping filter with different parameters.

In this paper, the actuator noise is set to be 0.1 μN/Hz$^{0.5}$. The sensor noises of x, y, x_1 and x_2 axis are both 1 nm/Hz$^{0.5}$. And the sensor noises of φ axis and x_2 axis are both 1 nrad/Hz$^{0.5}$. Corresponding to the scaling laws, the noises must be scaled up or scaled down. By setting the parameters in the above transfer function models, different coloured noises are generated and input into the system. The results of two groups of simulation experiments can be performed. And the

results of two groups of simulation experiments with corresponding scaled noises are presented in Fig. 12.

The red lines represent the results of Group 1. The green lines represent the results of Group 2. Compared with the simulation results without noises, the ground model system with equivalent thruster noise and sensor noise can simulate the space system more realistically. Different from the former results without noises, the new results show that the effect of control system is lightly reduced. But the difference is less marked and the trend of simulation results is the same. The simulation system with noises can still maintain stability.

Moreover, the scaling laws are applied to the above simulation results. The new scaled results can be obtained, as shown in Fig. 13.

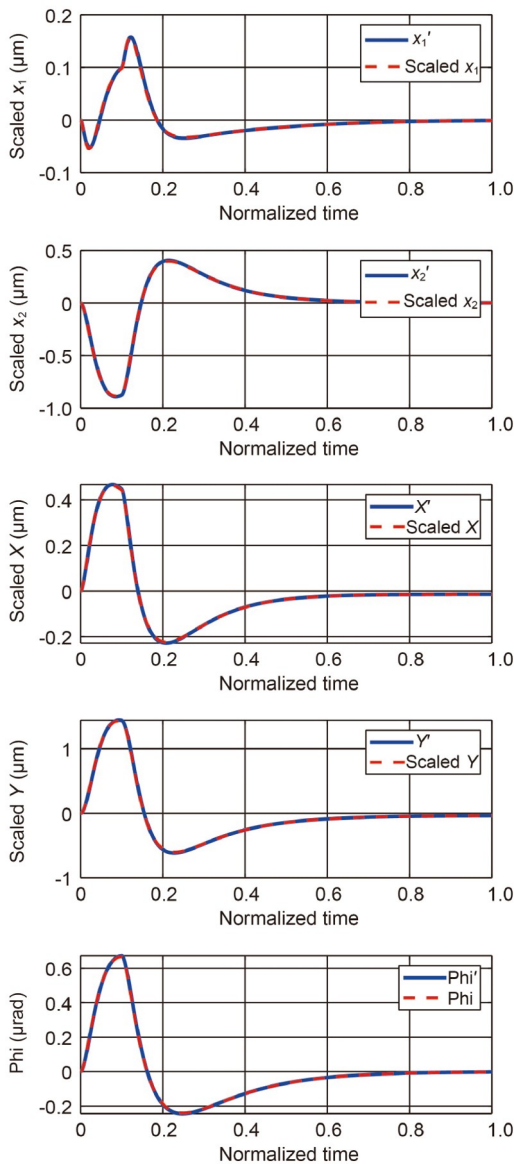The above pictures show the scaled simulation results.

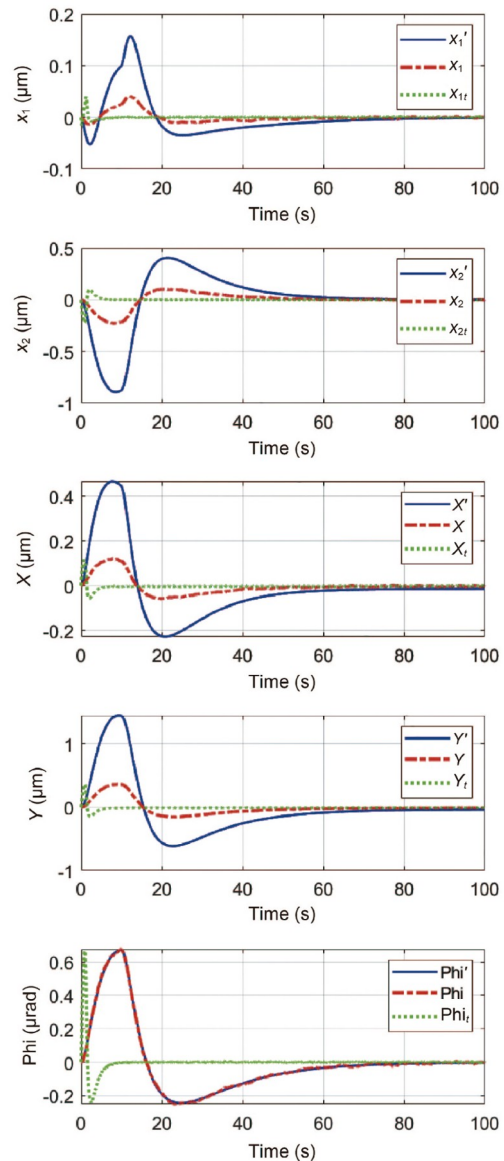**Figure 11** Results of prototype and scaled Group 2.

Figure 12 Results of prototype and Groups.

The red lines represent the results of scaled Group 1. The green lines represent the results of scaled Group 2. And it can be found that the motion trajectory of the model with thruster noises and sensor noises is not completely consistent with that of the prototype system. But the simulation results with noises are still similar, to a large extent, to results of the prototype system. It indicates that the equivalent similarity of the two systems still exists. The law of similarity can still be applied to the design of ground air-bearing floating simulator. In addition, the equivalent scaling results of thruster and sensor noise can be used to design actuators for ground model system tests, including thrust ranges and thrust noise.

6. Conclusion

For the ground physical simulation experiment of the space gravitational wave detection satellite, we put forward a similar design method of the scaled drag-free spacecraft simulator. A ground air-bearing simulator testbed with two test masses is designed to emulate the planar dynamics of the drag-free spacecraft. Through theoretical analysis and simulation experiments, the following conclusions are drawn:

(1) Based on dimensional analysis and π theorem, the dimensionless similarity criterion is established, representing the dynamic characteristics of the space drag-free satellite with two test masses. Dynamic equivalent conditions, determined by the similarity criterion, are deduced to construct the scaling laws which could make the model simulator be correctly scaled.

(2) We firstly proposed the concepts of the equivalent mass and equivalent stiffness of the inverted pendulum in this paper. By using these concepts, the equivalent dynamic model is deduced from the Euler-Lagrange method to verify the similarity between the ground model and the space prototype. And the necessary conditions, listed for designing the inverted pendulum equivalent to the test mass along the sensitive axis, are also derived theoretically.

(3) To address the problem of the underactuated system, a closed-loop control strategy of drag-free control in the displacement mode is devised and succeeds in manipulating the model simulator steadily. The comparative simulation experiments, involving control scaling laws and different scaling factors, demonstrate that both kinematic similarity and dynamic similarity hold true.

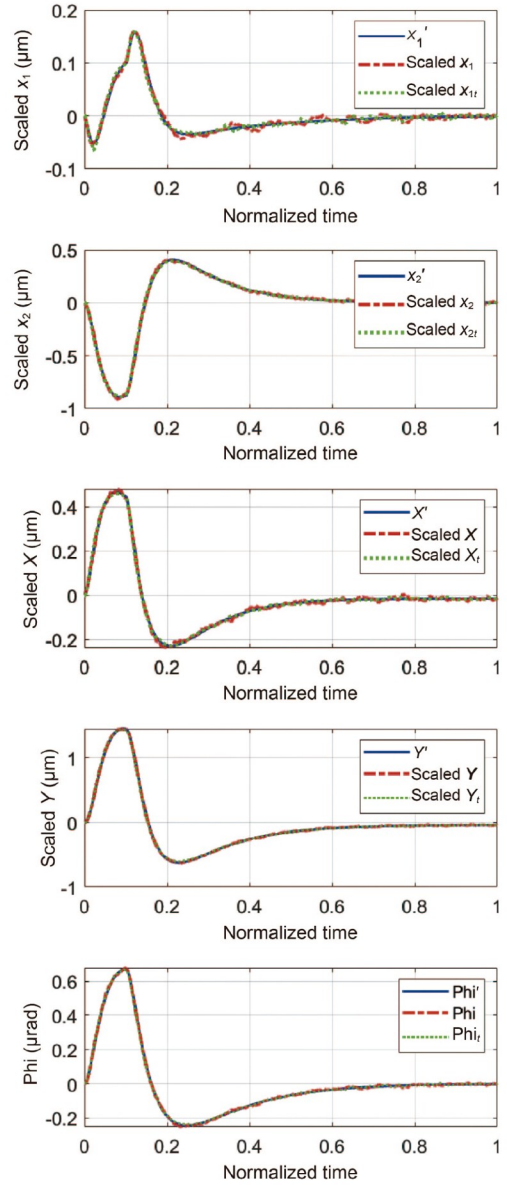(4) The research results demonstrate that the proposed

Figure 13 Results of prototype and scaled Groups.

design method is reasonable and effective, which can be used not only for the physical simulation research of space gravitational wave detection satellites, but also for the ground physical simulation research of other satellites orbiting the sun or the earth.

Appendix

$\mathbf{C}_{i/\mathrm{SC}}$ is the coordinate transformation matrix.

$$\mathbf{C}_{i/\mathrm{SC}} = \begin{bmatrix} 1 & 0 & 0 \\ 0 & \cos\theta_x & \sin\theta_x \\ 0 & -\sin\theta_x & \cos\theta_x \end{bmatrix} \begin{bmatrix} \cos\theta_y & 0 & -\sin\theta_y \\ 0 & 1 & 0 \\ \sin\theta_y & 0 & \cos\theta_y \end{bmatrix} \begin{bmatrix} \cos\theta_z & \sin\theta_z & 0 \\ -\sin\theta_z & \cos\theta_z & 0 \\ 0 & 0 & 1 \end{bmatrix}. \tag{A1}$$

$\mathbf{M}_{sc}$ and $\mathbf{m}_i$ are the generalized mass matrices of the testbed and the i-th inverted pendulum. $\dot{\mathbf{r}}_M$ and $\dot{\mathbf{r}}_{mi}$ are the generalized displacements vector of the testbed and the i-th inverted pendulum.

$$\mathbf{M}_{sc} = \begin{bmatrix} M & 0 & 0 \\ 0 & M & 0 \\ 0 & 0 & I_z \end{bmatrix}, \quad \mathbf{m}_i = \begin{bmatrix} m_i & 0 & 0 & 0 \\ 0 & m_i & 0 & 0 \\ 0 & 0 & I_{zi} & 0 \\ 0 & 0 & 0 & J_{mi} \end{bmatrix},$$

$$\dot{\mathbf{r}}_M = \begin{pmatrix} \dot{x} \\ \dot{y} \\ \dot{\varphi} \end{pmatrix}, \quad \dot{\mathbf{r}}_{mi} = \begin{pmatrix} \dot{x} - y_{pi}\dot{\varphi} - e_i\dot{\varphi}\sin\varphi_i\sin\theta_i - e_i\varphi\dot{\theta}_i\cos\theta_i\sin\varphi_i + e_i\dot{\theta}_i\cos\theta_i\cos\varphi_i \\ \dot{y} + x_{pi}\dot{\varphi} + e_i\dot{\varphi}\cos\varphi_i\sin\theta_i + e_i\varphi\dot{\theta}_i\cos\theta_i\cos\varphi_i + e_i\dot{\theta}_i\cos\theta_i\sin\varphi_i \\ \dot{\varphi} \\ \dot{\theta}_i \end{pmatrix}.$$

$$(A2)$$

The expressions of $\dot{\mathbf{r}}$, $\mathbf{M}$, $\mathbf{M}_{cp}$, $\mathbf{A}_1$ and $\mathbf{A}_2$ are as follows:

$$\dot{\mathbf{r}} = \begin{pmatrix} \dot{x} \\ \dot{y} \\ \dot{\varphi} \\ \dot{\theta}_1 \\ \dot{\theta}_2 \end{pmatrix}, \quad \mathbf{M} = \begin{bmatrix} M & 0 & 0 & 0 & 0 \\ 0 & M & 0 & 0 & 0 \\ 0 & 0 & I_z + I_{z1} + I_{z2} & 0 & 0 \\ 0 & 0 & 0 & J_{m1} & 0 \\ 0 & 0 & 0 & 0 & J_{m2} \end{bmatrix}, \quad \mathbf{M}_{cp} = \begin{bmatrix} 0 & 0 & 0 & 0 & 0 \\ 0 & 0 & 0 & 0 & 0 \\ 0 & 0 & 0 & 0 & 0 \\ 0 & 0 & 0 & m_1 & 0 \\ 0 & 0 & 0 & 0 & m_2 \end{bmatrix},$$

$$\mathbf{A}_1 = \begin{bmatrix} 0 & 0 & 0 & 0 & 0 \\ 0 & 0 & 0 & 0 & 0 \\ 0 & 0 & 0 & 0 & 0 \\ 1 & 0 & -y_{p1} - e_1\sin\theta_1\sin\varphi_1 & e_1\cos\theta_1(\cos\varphi_1 - \varphi\sin\varphi_1) & 0 \\ 1 & 0 & -y_{p2} - e_2\sin\theta_2\sin\varphi_2 & 0 & e_2\cos\theta_2(\cos\varphi_2 - \varphi\sin\varphi_2) \end{bmatrix}, \quad (A3)$$

$$\mathbf{A}_2 = \begin{bmatrix} 0 & 0 & 0 & 0 & 0 \\ 0 & 0 & 0 & 0 & 0 \\ 0 & 0 & 0 & 0 & 0 \\ 0 & 1 & e_1\sin\theta_1\cos\varphi_1 + x_{p1} & e_1\cos\theta_1(\sin\varphi_1 + \varphi\cos\varphi_1) & 0 \\ 0 & 1 & e_2\sin\theta_2\cos\varphi_2 + x_{p2} & 0 & e_2\cos\theta_2(\sin\varphi_2 + \varphi\cos\varphi_2) \end{bmatrix}.$$

$\mathbf{C}_g$ in Eq. (29) is

$$\mathbf{C}_g = \begin{bmatrix} m_1 e_1\cos\varphi_1 & m_1 e_1\sin\varphi_1 & m_1 e_1(x_{p1}\sin\varphi_1 - y_{p1}\cos\varphi_1) \\ m_2 e_2\cos\varphi_2 & m_2 e_2\sin\varphi_2 & m_2 e_2(x_{p2}\sin\varphi_2 - y_{p2}\cos\varphi_2) \end{bmatrix}.$$

$$(A4)$$

$\mathbf{C}_{tr}$ in Eq. (51) is

$$\mathbf{C}_{tr} = \begin{bmatrix} -\cos\varphi_1 & -\sin\varphi_1 & -x_{p1}\sin\varphi_1 + y_{p1}\cos\varphi_1 \\ -\cos\varphi_2 & -\sin\varphi_2 & -x_{p2}\sin\varphi_2 + y_{p2}\cos\varphi_2 \end{bmatrix}. \quad (A5)$$

$\mathbf{B}$ in Eq. (53) is

$$\mathbf{B} = \begin{bmatrix} -\sin\varphi_2 & \sin\varphi_1 & \sin\varphi_1(x_{p2}\sin\varphi_2 - y_{p2}\cos\varphi_2) - \sin\varphi_2(x_{p1}\sin\varphi_1 - y_{p1}\cos\varphi_1) \\ \cos\varphi_2 & -\cos\varphi_1 & \cos\varphi_1(x_{p2}\sin\varphi_2 - y_{p2}\cos\varphi_2) - \cos\varphi_2(x_{p1}\sin\varphi_1 - y_{p1}\cos\varphi_1) \\ 0 & 0 & \cos\varphi_1\sin\varphi_2 - \cos\varphi_2\sin\varphi_1 \end{bmatrix}. \quad (A6)$$

The calculation of $\mathbf{A}$, $\mathbf{A}^+$ and $\mathbf{A}^-$ are

$$\mathbf{A} = \begin{bmatrix} -0.7071 & -0.7071 & -0.7071 & 0.7071 & 0.7071 & 0.7071 & 0.7071 & -0.7071 \\ 0.7071 & -0.7071 & -0.7071 & -0.7071 & -0.7071 & 0.7071 & 0.7071 & 0.7071 \\ 0.2510 & -0.2510 & 0.2510 & -0.2510 & 0.2510 & -0.2510 & 0.2510 & -0.2510 \end{bmatrix},$$

$$\mathbf{A}^+ = \begin{bmatrix} 0 & 0.3535 & 0.9959 \\ 0 & 0 & 0 \\ 0 & 0 & 0.9959 \\ 0.3535 & 0 & 0 \\ 0.3535 & 0 & 0.9959 \\ 0.3535 & 0.3535 & 0 \\ 0.3535 & 0.3535 & 0.9959 \\ 0 & 0.3535 & 0 \end{bmatrix}, \quad \mathbf{A}^- = \begin{bmatrix} 0.3535 & 0 & 0 \\ 0.3535 & 0.3535 & 0.9959 \\ 0.3535 & 0.3535 & 0 \\ 0 & 0.3535 & 0.9959 \\ 0 & 0.3535 & 0 \\ 0 & 0 & 0.9959 \\ 0 & 0 & 0 \\ 0.3535 & 0 & 0.9959 \end{bmatrix}. \tag{A7}$$

1 B. Lange, The drag-free satellite, AIAA J. **2**, 1590 (1964).
2 B. Ziegler, and M. Blanke, in Drag-free motion control of satellite for high-precision gravity field mapping: Proceedings of the International Conference on Control Applications, Glasgow, 2002.
3 T. Edwards, M. C. W. Sandford, and A. Hammesfahr, LISA—a study of the ESA cornerstone mission for observing gravitational waves, Acta Astronaut. **48**, 549 (2001).
4 W. R. Hu, and Y. L. Wu, The Taiji Program in Space for gravitational wave physics and the nature of gravity, Natl. Sci. Rev. **4**, 685 (2017).
5 W. H. Ruan, C. Liu, Z. K. Guo, Y. L. Wu, and R. G. Cai, The LISA–Taiji network, Nat. Astron. **4**, 108 (2020).
6 J. Luo, L. S. Chen, H. Z. Duan, Y. G. Gong, S. Hu, J. Ji, Q. Liu, J. Mei, V. Milyukov, M. Sazhin, C. G. Shao, V. T. Toth, H. B. Tu, Y. Wang, Y. Wang, H. C. Yeh, M. S. Zhan, Y. Zhang, V. Zharov, and Z. B. Zhou, TianQin: A space-borne gravitational wave detector, Class. Quantum Grav. **33**, 035010 (2016).
7 H. Bock, A. Jäggi, G. Beutler, and U. Meyer, GOCE: Precise orbit determination for the entire mission, J. Geod. **88**, 1047 (2014).
8 J. Li, W. J. Bencze, D. B. DeBra, G. Hanuschak, T. Holmes, G. M. Keiser, J. Mester, P. Shestople, and H. Small, On-orbit performance of Gravity Probe B drag-free translation control and orbit determination, Adv. Space Res. **40**, 1 (2007).
9 A. Schleicher, T. Ziegler, R. Schubert, N. Brandt, P. Bergner, U. Johann, W. Fichter, and J. Grzymisch, In-orbit performance of the LISA Pathfinder drag-free and attitude control system, CEAS Space J. **10**, 471 (2018).
10 Y. L. Wu, Z. R. Luo, J. Y. Wang, M. Bai, W. Bian, R. G. Cai, Z. M. Cai, J. Cao, D. J. Chen, L. Chen, L. S. Chen, M. W. Chen, W. B. Chen, Z. Y. Chen, L. X. Cong, J. F. Deng, X. L. Dong, L. Duan, S. Q. Fan, S. S. Fan, C. Fang, Y. Fang, K. Feng, P. Feng, Z. Feng, R. H. Gao, R. L. Gao, Z. K. Guo, J. W. He, J. B. He, X. Hou, L. Hu, W. R. Hu, Z. Q. Hu, M. J. Huang, J. J. Jia, K. L. Jiang, G. Jin, H. B. Jin, Q. Kang, J. G. Lei, B. Q. Li, D. J. Li, F. Li, H. S. Li, H. W. Li, L. F. Li, W. Li, X. K. Li, Y. M. Li, Y. G. Li, Y. P. Li, Y. P. Li, Z. Li, Z. Y. Lin, C. Liu, D. B. Liu, H. S. Liu, H. Liu, P. Liu, Y. R. Liu, Z. Y. Lu, H. W. Luo, F. L. Ma, L. F. Ma, X. S. Ma, X. Ma, Y. C. Man, J. Min, Y. Niu, J. K. Peng, X. D. Peng, K. Q. Qi, L. É. Qiang, C. F. Qiao, Y. X. Qu, W. H. Ruan, W. Sha, J. Shen, X. J. Shi, R. Shu, J. Su, Y. L. Sui, G. W. Sun, W. L. Tang, H. J. Tao, W. Z. Tao, Z. Tian, L. F. Wan, C. Y. Wang, J. Wang, J. Wang, L. L. Wang, S. X. Wang, X. P. Wang, Y. K. Wang, Z. Wang, Z. L. Wang, Y. X. Wei, Y. X. Di Wu, L. M. Wu, P. Z. Wu, Z. H. Wu, D. X. Xi, Y. F. Xie, G. F. Xin, L. X. Xu, P. Xu, S. Y. Xu, Y. Xu, S. W. Xue, Z. B. Xue, C. Yang, R. Yang, S. J. Yang, S. Yang, Y. Yang, Z. G. Yang, Y. L. Yin, J. P. Yu, T. Yu, À. B. Zhang, C. Zhang, M. Zhang, X. Q. Zhang, Y. Z. Zhang, J. Zhao, W. W. Zhao, Y. Zhao, J. H. Zheng, C. Y. Zhou, Z. C. Zhu, X. B. Zou, and Z. M. Zou, China's first step towards probing the expanding universe and the nature of gravity using a space borne gravitational wave antenna, Commun. Phys. **4**, 34 (2021).
11 L. Wu, P. Xu, S. Zhao, L. E. Qiang, Z. Luo, and Y. Wu, Global gravity field model from Taiji-1 observations, Microgravity Sci. Technol. **34**, 77 (2022).
12 A. S. Pau, A. Heather, B. Stanislav, B. John, B. Enrico, B. Peter, B. Emanuele, B. Pierre, B. Michael, B. Daniele, C. Jordan, C. Chiara, C. Vitor, C. Monica, C. John, C. Neil, C. Curt, D. Karsten, D. Rita, F. Luigi, F. Valerio, F. Ewan, G. Jonathan, G. B. Lluis, G. Domenico, G. Ferran, G. Catia, H. Hubert, H. Gerhard, H. Tho-Thomas, H. Martin, H. B. Kelly, H. Daniel, H. Mauro, I. Henri, J. Philippe, K. Nikos, K. Christian, K. Antoine, K. Bill, K. Natalia, L. L. Shane, L. Jeffrey, L. Ivan, M. Nary, M. Davor, M. Joseph, M. Ignacio, M. K. Kirk, T. M. W. Sean, M. Cole, M. Guido, N. Germano, N. Gijs, N. Miquel, P. Antoine, P. Paolo, P. Eric, P. Ed, R. Jens, R. David, R. Norna, R. Elena, R. Giuliana, S. Bernard, S. Alberto, S. David, S. Jacob, F. S. Carlos, S. Tim, T. Nicola, T. Ira, T. Michael, V. Michele, V. Alberto, V. Daniele, V. Stefano, V. Marta, W. Gudrun, W. Harry, W. Peter, W. William, Z. John, and Z. Peter, Laser interferometer space antenna, arXiv: 1702.00786.
13 Z. Luo, Y. Wang, Y. Wu, W. Hu, and G. Jin, The Taiji program: A concise overview, Prog. Theor. Exp. Phys. **2021(5)**, 05A108 (2021).
14 Y. Gong, J. Luo, and B. Wang, Concepts and status of Chinese space gravitational wave detection projects, Nat. Astron. **5**, 881 (2021).
15 I. Kawano, M. Mokuno, T. Kasai, and T. Suzuki, First autonomous rendezvous using relative GPS navigation by ETS-VII, Navigation **48**, 49 (2001).
16 M. Wilde, C. Clark, and M. Romano, Historical survey of kinematic and dynamic spacecraft simulators for laboratory experimentation of on-orbit proximity maneuvers, Prog. Aerospace Sci. **110**, 100552 (2019).
17 X. L. Ding, Y. C. Wang, Y. B. Wang, and K. Xu, A review of structures, verification, and calibration technologies of space robotic systems for on-orbit servicing, Sci. China Tech. Sci. **64**, 462 (2021).
18 A. Caon, F. Branz, and A. Francesconi, Development and test of a robotic arm for experiments on close proximity operations, Acta Astronaut. **195**, 287 (2022).
19 L. Zong, and M. R. Emami, Control verifications of space manipulators using ground platforms, IEEE Trans. Aerosp. Electron. Syst.

M. Chen, *et al. Acta Mech. Sin.*, Vol. 41, 524026 (2025)

524026-19

57, 341 (2021).

20 S. B. McCamish, M. Romano, S. Nolet, C. M. Edwards, and D. W. Miller, Flight testing of multiple-spacecraft control on SPHERES during close-proximity operations, J. Spacecraft Rockets **46**, 1202 (2009).

21 C. Menon, A. Aboudan, S. Cocuzza, A. Bulgarelli, and F. Angrilli, Free-flying robot tested on parabolic flights: Kinematic control, J. Guidance Control Dyn. **28**, 623 (2005).

22 C. Zhang, C. Yang, L. Hu, S. Chen, Y. Zhao, L. Duan, and Q. Kang, Beijing drop tower microgravity adjustment towards $10^{-3} \sim 10^{-5}$ g level by cold-gas thrusters, Microgravity Sci. Technol. **35**, 39 (2023).

23 S. Chesi, O. Perez, and M. Romano, A dynamic, hardware-in-the-Loop, three-axis simulator of spacecraft attitude maneuvering with nanosatellite dimensions, J. Small Spacecraft. **4**, 315 (2015).

24 M. Ciarcià, R. Cristi, and M. M. Romano, Emulating scaled Clohessy-Wiltshire dynamics on an air-bearing spacecraft simulation testbed, J. Guidance Control Dyn. **40**, 2496 (2017).

25 Y. Eun, S. Y. Park, and G. N. Kim, Development of a hardware-in-the-loop testbed to demonstrate multiple spacecraft operations in proximity, Acta Astronaut. **147**, 48 (2018).

26 B. R. Fernandez, L. Herrera, J. Hudson, and M. Romano, Development of a tip-tilt air-bearing testbed for physically emulating proximity-flight orbital mechanics, Adv. Space Res. **71**, 4332 (2023).

27 C. Zhang, J. He, M. Chen, L. Duan, and Q. Kang, Ground semi-physical simulation experiment study of one-dimensional drag-free control, Int. J. Mod. Phys. A **36**, 2140016 (2021).

28 C. Yang, J. W. He, L. Duan, and Q. Kang, A torsional thrust stand for measuring the thrust response time of micro-Newton thrusters, Int. J. Mod. Phys. A **36**, 2140015 (2021).

29 A. Sonin, The Physical Basis of Dimensional Analysis, 2nd ed. (Department of Mechanical Engineering, MIT, Cambridge, 2001). pp. 29-43.

30 E. Buckingham, On physically similar systems; illustrations of the use of dimensional equations, Phys. Rev. **4**, 345 (1914).

31 I. I. Zappulla Richard, J. Virgili-Llop, C. Zagaris, H. Park, and M. Romano, Dynamic air-bearing hardware-in-the-loop testbed to experimentally evaluate autonomous spacecraft proximity maneuvers, J. Spacecraft Rockets **54**, 825 (2017).

32 N. M. J. Woodhouse, Lagrangian mechanics, in: Introduction to Analytical Dynamics: Revised Edition, edited by N. Woodhouse (Springer, London, 2009). pp. 67-98.

33 A. Naceri, N. Boccardo, L. Lombardi, A. Marinelli, D. Hidalgo, S. Haddadin, M. Laffranchi, and L. De Michieli, From human to robot grasping: Force and kinematic synergies, in: Tactile Sensing, Skill Learning, and Robotic Dexterous Manipulation (Elsevier, 2022). pp. 133-148.

34 T. A. Johansen, and T. I. Fossen, Control allocation—A survey, Automatica **49**, 1087 (2013).

等效模拟无拖曳卫星动力学的地面气浮装置相似设计方法

陈明伟, 章楚, 贺建武, 杨超, 段俐, 康琦

摘要 为了设计无拖曳卫星相关技术演示验证的地面仿真平台, 本文基于量纲分析和π理论等方法提出了一种与空间无拖曳卫星平面动力学行为相似的地面模型设计方法. 该方法从双检验质量无拖曳卫星动力学模型中分析出相似特征, 设计了由倒立摆和平面气浮台组成的地面气浮模拟装置. 文中利用欧拉-拉格朗日方法推导了等效于检验质量敏感轴平动和卫星平面运动的模拟器动力学模型, 得出地面模型系统等效空间原型系统的动力学等效条件. 此外, 本文首次提出了等效质量和等效刚度的概念, 并在此基础上提出了满足等效条件的相似律设计要求以及倒立摆的设计要求. 在物理相似性条件下, 本文设计了欠驱动系统的闭环控制策略, 推导出相应的控制相似律并应用于数值仿真. 最后, 等效缩放后仿真结果与原型仿真结果的对比验证了二者动力学行为具有相似性, 也证明了本文提出的相似性设计方法的合理性和有效性, 为未来引力波探测计划的无拖曳卫星地面仿真设计提供了更多依据.